AGU PUBLICATIONS

JGR

Journal of Geophysical Research: Atmospheres

RESEARCH ARTICLE
10.1002/2015JD024354

Key Points:
- This model decomposes LST time series into trend, seasonal, and noise components
- This model simultaneously detects seasonal, gradual, and abrupt changes of LST
- SUHII in Beijing showed a growing trend and a concave seasonal pattern at night

Supporting Information:
- Supporting Information S1

Correspondence to:
Y. Chen,
cyh@bnu.edu.cn

Citation:
Quan, J., W. Zhan, Y. Chen, M. Wang, and J. Wang (2016), Time series decomposition of remotely sensed land surface temperature and investigation of trends and seasonal variations in surface urban heat islands, *J. Geophys. Res. Atmos.*, *121*, 2638–2657, doi:10.1002/2015JD024354.

Received 19 OCT 2015
Accepted 27 FEB 2016
Accepted article online 4 MAR 2016
Published online 24 MAR 2016

Time series decomposition of remotely sensed land surface temperature and investigation of trends and seasonal variations in surface urban heat islands

Jinling Quan[1,2], Wenfeng Zhan[3], Yunhao Chen[2], Mengjie Wang[2], and Jinfei Wang[4]

[1]State Key Laboratory of Resources and Environmental Information System, Institute of Geographic Sciences and Natural Resources Research, Chinese Academy of Sciences, Beijing, China, [2]State Key Laboratory of Earth Surface Processes and Resource Ecology, College of Resources Science and Technology, Beijing Normal University, Beijing, China, [3]Jiangsu Provincial Key Laboratory of Geographic Information Science and Technology, International Institute for Earth System Science, Nanjing University, Nanjing, Jiangsu, China, [4]Department of Geography, University of Western Ontario, London, Ontario, Canada

Abstract Previous time series methods have difficulties in simultaneous characterization of seasonal, gradual, and abrupt changes of remotely sensed land surface temperature (LST). This study proposed a model to decompose LST time series into trend, seasonal, and noise components. The trend component indicates long-term climate change and land development and is described as a piecewise linear function with iterative breakpoint detection. The seasonal component illustrates annual insolation variations and is modeled as a sinusoidal function on the detrended data. This model is able to separate the seasonal variation in LST from the long-term (including gradual and abrupt) change. Model application to nighttime Moderate Resolution Imaging Spectroradiometer (MODIS)/LST time series during 2000–2012 over Beijing yielded an overall root-mean-square error of 1.62 K between the combination of the decomposed trend and seasonal components and the actual MODIS/LSTs. LST decreased (~ -0.086 K/yr, $p < 0.1$) in 53% of the study area, whereas it increased with breakpoints in 2009 (~0.084 K/yr before and ~0.245 K/yr after 2009) between the fifth and sixth ring roads. The decreasing trend was stronger over croplands than over urban lands ($p < 0.05$), resulting in an increasing trend in surface urban heat island intensity (SUHII, 0.022 ± 0.006 K/yr). This was mainly attributed to the trends in urban-rural differences in rainfall and albedo. The SUHII demonstrated a concave seasonal variation primarily due to the seasonal variations of urban-rural differences in temperature cooling rate (related to canyon structure, vegetation, and soil moisture) and surface heat dissipation (affected by humidity and wind).

1. Introduction

Land surface temperature (LST) is a key variable in global and regional climate changes, hydrological cycles, and surface-atmosphere interactions [*Voogt and Oke*, 2003; *Li et al.*, 2013]. Characterizing changes in LST is increasingly important for understanding the present environmental conditions and predicting or managing future changes [*Watts and Laffan*, 2014]. Changes in LST occur on multiple timescales, which can be generally divided into four groups: interannual, seasonal, diurnal, and abrupt changes [*Verbesselt et al.*, 2010; *Zhan et al.*, 2014a]. Here we mainly focus on the changes with a timescale no shorter than 1 day.

Thermal infrared remote sensing has been widely used to detect changes in LST due to its advantages of wide coverage, repeatable orbit cycle, and low cost. However, due to clouds, heavy aerosols, systematic errors, and other disturbances, missing values commonly exist in satellite thermal images [*Hu and Brunsell*, 2013; *Quan et al.*, 2014a]. To avoid the missing data, many studies have selected a small number of clear-sky images for intercomparison [*Coppin et al.*, 2004]. However, this image sampling has the following issues:

1. Large uncertainties may be induced due to various instantaneous influences, subjective selection, and image representativeness and comparability. This may lead to different or even controversial results for the same study area.
2. Normalization/summarization of the data needs to be preconducted, or a reference period or a change trajectory/threshold must be predetermined [*Lu et al.*, 2004].
3. Only one category of change can be detected at one time [*Coppin et al.*, 2004], and the intermediate change or the change of interest is frequently lost [*de Beurs and Henebry*, 2005].

To circumvent the aforementioned shortcomings, time series analysis methods have been proposed to quantify continuous temporal variations in LST. Many of these methods are only designed or tested for vegetation response, e.g., the normalized difference vegetation index (NDVI), and are considered to be applicable to LST time series, given their relationship and similar signal composition forms. These methods include the seasonal trend decomposition procedure based on locally weighted regression smoother [*Cleveland et al*., 1990], Fourier transform [*Menenti et al*., 1993; *Verhoef et al*., 1996; *Roerink et al*., 2000], asymmetric Gaussian function [*Jönsson and Eklundh*, 2002], logistic function [*Beck et al*., 2006], wavelet transform [*Galford et al*., 2008], breaks for additive seasonal and trend [*Verbesselt et al*., 2010], principal component analysis (PCA)/empirical orthogonal function [*Small*, 2012], and detecting breakpoints and estimating segments in trend [*Jamali et al*., 2015]. Nevertheless, at least one of the following challenges remains: (1) only the seasonal variation is taken into account, whereas the long-term variation is neglected or the abrupt change cannot be detected, and vice versa; (2) identification of each dimension/component obtained from the Fourier transform, wavelet transform, PCA, etc. is challenging because the analysis depends entirely on the thermal image series used [*Verbesselt et al*., 2010]; and (3) tests on LST time series have yet to be widely conducted and the model feasibility can hardly be asserted.

Several other studies have modeled the annual cycle of LST time series by directly fitting a harmonic function [*Thomson*, 1995; *Eliseev and Mokhov*, 2003; *Bechtel*, 2012; *Weng and Fu*, 2014; *Zhan et al*., 2014a]. However, the LST time series are practically cyclostationary for annual temperature cycle modeling only after the interannual and abrupt changes are excluded [*Zhang and Qi*, 2005; *Halliday et al*., 2012]. And these changes cannot be neglected without prior knowledge [*Parey et al*., 2013].

This study proposed an LST time series decomposition method to extract trend, seasonal, and noise components for simultaneously characterizing the seasonal variation while detecting the long-term (gradual and abrupt) change. This method is termed the trend and seasonal decomposition model (TSDM) here. We assessed TSDM by simulated data for a range of land covers and actual Moderate Resolution Imaging Spectroradiometer (MODIS)/LST time series over Beijing during 2000–2012. Instead of solely focusing on the newly developed model, we further investigated trends and seasonal patterns of the surface urban heat island (SUHI) intensity (SUHII) based on the results of the TSDM. This investigation was primarily motivated by the rare use of LST trend analysis to study SUHI to date.

Furthermore, contributions of several selected biophysical variables to the temporal changes in LST and SUHII were analyzed for the purpose of better understanding the thermal environmental change and suggesting potential remediation for urban heat effects. Unlike many previous studies [*Lo et al*., 1997; *Gallo and Owen*, 1998; *Chen et al*., 2006; *Jenerette et al*., 2007; *Yuan and Bauer*, 2007; *Jin et al*., 2011; *Peng et al*., 2012; *Zhou et al*., 2014], we highlight variations of urban-rural differences in driving factor on interannual and seasonal scales in parallel with the trends and seasonal changes of SUHII, respectively.

2. Method

2.1. Trend and Seasonal Decomposition Model

2.1.1. General Model

We propose a method that decomposes remotely sensed LST time series $T(t)$ (t is the time) into trend, seasonal, and noise components ($T_t(t)$, $T_s(t)$, and $T_n(t)$, respectively). The trend component describes a gradual change in LST at a timescale longer than 1 year (which may include abrupt changes), indicating climate change and land development and management [*Verbesselt et al*., 2010]. The seasonal component is a regular and periodic change in LST on an annual scale, primarily driven by the annual variation in insolation [*Zhan et al*., 2014a, 2014b]. The noise component is a stochastic and irregular variation in LST that is caused by observation conditions (e.g., view angle and signal-to-noise ratio), atmospheric environments (e.g., clouds and aerosols), and disturbance events (e.g., fire and flood). The three components are considered to be additive, so that

$$T(t) = T_t(t) + T_s(t) + T_n(t). \quad (1)$$

The additivity may not be true, given that the components may not be independent or noninteracting [*Hylleberg*, 1994]. However, this assumption is necessary for achieving the component separability. The trend component $T_t(t)$ is extracted from the LST time series first, and then the seasonal component $T_s(t)$ is modeled

using the detrended data. This is because (1) for trend detection, seasonal trend time series resulted in better performance than deseasonalized time series [*Forkel et al*., 2013] and (2) for seasonal modeling, detrended time series are considered stationary and more appropriate than seasonal trend time series [*Zhang and Qi*, 2005]. The residuals are regarded as the noise component $T_n(t)$.

2.1.2. Trend Component

The trend component is described as a piecewise linear function, as given by equation (2). This is the most common practice to detect trends in time series analysis of biophysical variables [*de Beurs and Henebry*, 2005; *Verbesselt et al*., 2010; *Thanasis et al*., 2011; *Vergni and Todisco*, 2011; *Halliday et al*., 2012] because it can extract the fundamental features of data and reduce the complexity of fitting curves [*Zeileis et al*., 2003].

$$T_t(t) = a_i t + b_i, t \in (t_{i-1}, t_i), i = 1, 2, \ldots, I \tag{2}$$

where t_i is the position of the breakpoint, I is the total number of the breakpoints, and a_i and b_i are the slope and intercept of the linear function during each subperiod ($t_{i-1} < t \leq t_i$), respectively. The slope reveals the change magnitude. The breakpoint indicates an abrupt change in LST that may be caused by abrupt changes in climate and anthropogenic impact.

The ordinary least squares residuals-based moving sum (OLS-MOSUM) test is used to determine whether breakpoints occur in the LST time series [*Zeileis et al*., 2003]. If the OLS-MOSUM test indicates significant structural changes ($p < 0.05$), then the number and positions of breakpoints are iteratively estimated by minimizing the Bayesian information criterion and the sum of the regression residual squares, respectively [*Bai and Perron*, 2003]. A linear regression is then conducted during each subperiod. If the OLS-MOSUM test indicates no structural change, then a single linear regression is implemented throughout the whole period of time series. Given that the OLS-MOSUM test requires time series with an equal interval without missing values [*Verbesselt et al*., 2010], linear interpolation is preperformed to fill the gaps.

2.1.3. Seasonal Component

The seasonal component is represented by a widely used sinusoidal function, as given by equation (3) [*Thomson*, 1995; *Eliseev and Mokhov*, 2003; *Bechtel*, 2012; *Weng and Fu*, 2014; *Zhan et al*., 2014a]. Its theoretical basis is that the annual temperature cycle at a given latitude is primarily attributed to the annual oscillation of solar radiation received by the Earth [*Laskar et al*., 1993; *Thomson*, 1995; *Huang et al*., 1996].

$$T_s(t) = A \sin(2\pi f(t - t_0) + \theta) \tag{3}$$

where A is the seasonal amplitude; t_0 is the starting date of the annual temperature cycle, set as the spring equinox [*Weng and Fu*, 2014]; f is the frequency, set as a constant (1/365) considering one tropical year period [*Thomson*, 1995]; and θ is the phase shift.

The two unknown parameters (A and θ) are related to environmental conditions (e.g., solar luminosity, climate zone, atmospheric circulation, and water vapor), surface properties (e.g., topography, vegetation cover, albedo, and soil moisture), and anthropogenic intervention [*Thomson*, 1995; *Eliseev and Mokhov*, 2003; *Knutti et al*., 2006; *Stine et al*., 2009]. These two parameters can be determined using an unconstrained Levenberg-Marquardt minimization with a universal optimization [*Göttsche and Olesen*, 2001; *Quan et al*., 2014b] on the detrended data.

2.2. SUHII and Correlation Analysis

SUHII is the most classical indicator for a SUHI phenomenon [*Schwarz et al*., 2011; *Quan et al*., 2014a]. In this study, the trend/seasonal variation in the SUHII was defined as the difference between the urban and rural averages of the decomposed trend/seasonal components. The urban areas were determined as the urban and built-up lands within the sixth ring road in Beijing, while the rural areas were defined as the croplands within a radius of 40 km from the city center (Figure 2). High elevations (elevation > 100 m) and water pixels were excluded. This urban-rural discrimination was adopted on all of the images for achieving interannual/seasonal comparability [*Imhoff et al*., 2010; *Peng et al*., 2012; *Clinton and Gong*, 2013; *Zhou et al*., 2014].

Two land surface descriptors and six climate descriptors, i.e., NDVI, white-sky albedo (WSA), air temperature (AT), diurnal air temperature range (DATR), total rainfall (RF), relative humidity (RHU), wind speed (WIN), and sunshine duration (SSD), were selected to examine the possible drivers of the temporal patterns of LST. Their difference variables between the urban and rural areas (i.e., $\triangle$NDVI, $\triangle$WSA, $\triangle$AT, $\triangle$DATR, $\triangle$RF, $\triangle$RHU, $\triangle$WIN, and $\triangle$SSD) were calculated in parallel with SUHII. WSA is the bihemispherical reflectance, while black-sky albedo is

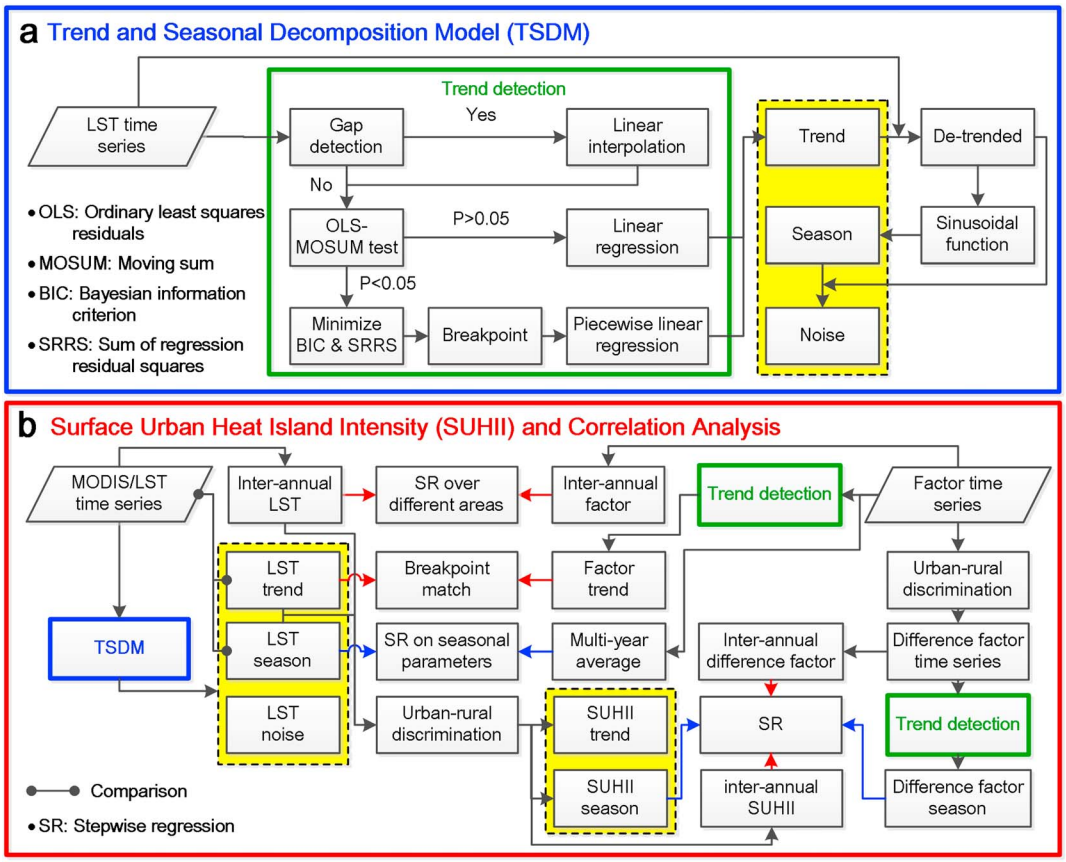

Figure 1. Flowchart of the method (a) presenting the procedure of TSDM in section 2.1 and (b) summarizing the process of SUHII and correlation analysis in section 2.2.

the directional hemispherical reflectance, which is linearly correlated with WSA [*Zhou et al.*, 2014; *Peng et al.*, 2012] and was therefore not included. First, the trend detection was individually applied to the eight (difference) factor time series, and the detrended data were considered as their seasonal components. Then, the breakpoints of LST were compared with those of NDVI and WSA, and the seasonal parameters (i.e., seasonal amplitude and phase shift) were individually correlated with the multiyear averaged NDVI and WSA using stepwise linear regression. Furthermore, annual composite was obtained from the deseasonalized LST time series and correlated with the annual composite of the eight factors by stepwise regression over urban, rural, and mountainous areas, respectively. Finally, stepwise regression was implemented between SUHII and the eight difference variables on interannual and seasonal scales, respectively. The relationship obtained on an interannual scale was considered applicable to the trends in LST and SUHII.

Methods in this section are illustrated in Figure 1.

3. Data

3.1. MODIS Data

Daily nighttime LST products from Terra/MODIS with a spatial resolution of 1 km (MOD11A1 in version 5) from March 2000 to December 2012 over Beijing (39°28′N to 41°05′N, 115°25′E to 117°30′E), China (Figure 2), were obtained at NASA's Earth Observing System and Data and Information System (EOSDIS) (https://earthdata.nasa.gov/). MOD11A1 was retrieved from clear-sky (99% confidence) observations [*Zhou et al.*, 2014] acquired at ~22:00 local solar time [*Quan et al.*, 2014a] using a generalized split-window algorithm [*Wan and Dozier*, 1996]. The accuracy is reported to be within 2 K over most homogeneous surfaces [*Wan*, 2014]. LSTs severely contaminated by clouds and thick aerosols were mostly removed [*Wan*, 2014]. This type of product was chosen because (1) it had the largest number of valid values over the study area among MODIS four-time

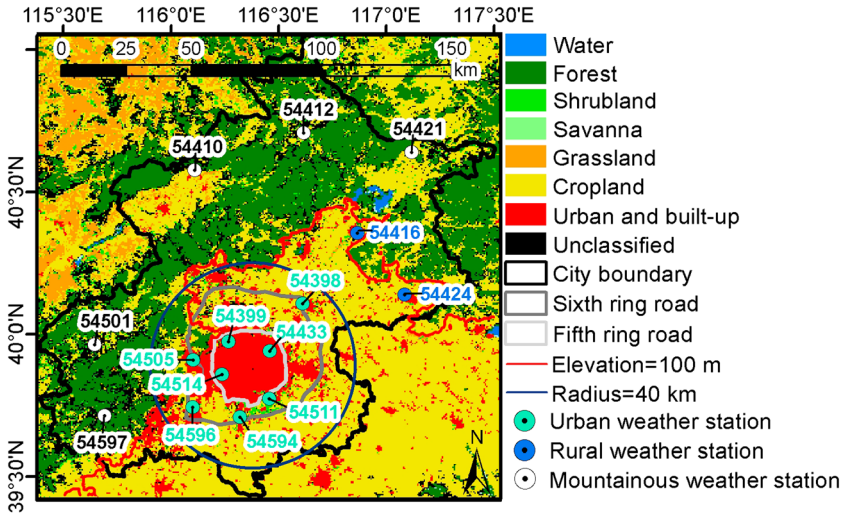

Figure 2. Study area. The land covers were combined from the MODIS yearly classification product in type 1 in 2009 (Figure 3). The red line is the boundary of regions with elevations smaller than 100 m in the south and east sides. The dark blue line is a circle region with a radius of 40 km from the city center.

(i.e., ~11:00, ~13:00, ~22:00, and ~02:00) observations [*Quan et al.*, 2014a]; (2) the correlation between LST and AT is stronger at night [*Voogt and Oke*, 2003; Nichol, 2005], which contributes to revealing the climate change using LST; and (3) the nighttime urban thermal environment is markedly related to the sleep condition [*Mackey et al.*, 2012], which highly affects residents' well-being.

We also collected MODIS NDVI (MOD13A3, monthly composite) and white-sky albedo (MCD43B3, 16 day composite) products over Beijing during 2000–2012 at the EOSDIS (https://earthdata.nasa.gov/). Both have a spatial resolution of 1 km. MOD13A3 is a weighted average value (in the case of cloud free) or a maximum value (in the case of clouds) of all 16 day NDVI that is calculated from atmospherically corrected red and near-infrared reflectance from Terra/MODIS [*Yang and Wang*, 2011]. MCD43B3 is generated according to the 16 day anisotropy model provided in the Terra and Aqua combined BRDF/Albedo Model Parameter product, and it indicates an average of the underlying 500 m values [*Yang and Wang*, 2011]. A more detailed description of the study area and the aforementioned MODIS products is available in the study by *Quan et al.* [2014a, 2014b].

For statistics of the results by land cover, MODIS yearly classification products in type 1 with a spatial resolution of 500 m (MCD12Q1) over Beijing from 2000 to 2012 were obtained at the EOSDIS (https://earthdata.nasa.gov/). MCD12Q1 has a classification scheme of 17 classes, which were combined into seven classes in this study for better statistical analysis [*Duan et al.*, 2014]. The combination is shown in Figure 3, where the snow/ice and barren/sparsely vegetated classes were precluded due to their extremely small sample size over the study area. The combined MCD12Q1 products were then aggregated to 1 km to match the MODIS/LST pixels [*Duan et al.*, 2014]. A total of 13 369 pixels (42%) without any land cover change during the 13 years was used for the statistics by land cover, where the savanna class was not included.

After combination	Before combination	
Water	Water	Wetlands
Forest	Evergreen needleleaf forest	Evergreen broadleaf forest
	Deciduous needleleaf forest	Deciduous broadleaf forest
	Mixed forest	
Shrubland	Closed shrublands	Open shrublands
Grassland	Grasslands	
Cropland	Croplands	Cropland mosaics
Built-up	Urban and built-up	
Savanna	Woody savannas	Savannas
Excluded	Snow/ice	Barren/sparsely vegetated

Figure 3. Combination of land cover types of MODIS yearly classification product in type 1.

3.2. Meteorological Data

Meteorological data sets (i.e., air temperature, diurnal air temperature range, total rainfall, relative humidity, wind speed, and sunshine duration) during 2000–2012 were collected from 15 Beijing meteorological stations (Figure 2) through the China Meteorological Data Sharing Service System (http://cdc.cma.gov.cn/home.do). To conduct correlations separately, the 15 weather stations

Table 1. Parameter Values for Various Simulated Cases

Parameters	Basic Data	Step [Range] Enumeration
Breakpoint number	2	- [-] -
Dates of two breakpoints	1 May 2004 and 31 Aug 2008	- [1 Jan 2002, 31 Dec 2010] 1 May 2004 and 31 Aug 2008; 1 Jan 2002 and 1 Jan 2004; 1 Jan 2006 and 1 Jan 2008; 31 Dec 2008 and 31 Dec 2010; 1 Jan. 2002 and 31 Dec 2010
Trend slopes in three subperiods (K/d)	0.003, −0.003, 0.0	0.001 [−0.003, 0.003] -
Averages of trends in three subperiods (K)	278, 278, 278	- [273, 283] -
Seasonal amplitude (K)	15	5 [5, 30] -
Phase shift (day)	0	10 [−50, 50] -
Noise level (K)	2	0.5 [0, 5] -

were classified into three categories according to their underlying surface types, elevations, and locations: urban (urban and built-up lands, elevation $<$ 100 m, within the sixth ring road), rural (croplands, elevation $<$ 100 m, outside of the sixth ring road), and mountainous (forest/shrublands/savannas/grasslands, elevation $>$ 100 m, outside of the sixth ring road).

3.3. Simulated Data

To robustly test TSDM in a controlled environment, we simulated daily LST time series throughout 13 years (i.e., 2000–2012) with different positions of breakpoints, trend slopes, seasonal amplitudes, phase shifts, and noise levels for representing a range of land cover types (Table 1). Most of the parameter values were determined based on the decomposed results of the MODIS/LST time series over Beijing (see Text S1 of the supporting information for detail). In the random cases, parameters were randomly generated within their valid ranges, while in the other cases, only one parameter value was changed step by step and the other parameters were kept the same as the basic data (Table 1). Then, the trend, seasonal, and noise components were calculated individually according to equations (2) and (3) and a normal function (0, σ) [*Cleveland et al.*, 1990]. Finally, the simulated LST time series were generated using equation (1). Figure 4 shows an example of the simulated LST time series.

4. Model Analysis Based on Simulated Data

4.1. With Various Trend, Seasonal, and Noise Parameters

Figure 4 shows great similarity between the simulated and decomposed trend and seasonal components. To quantitatively assess the model performance, root-mean-square errors (RMSEs) between the decomposed and simulated trend/seasonal components and absolute differences (ADs) between the derived and simulated seasonal amplitudes/phase shifts under various simulated cases (Table 1) were calculated, as shown in Figure 5. Each case has one pair of derived and simulated seasonal amplitudes/phase shifts, and

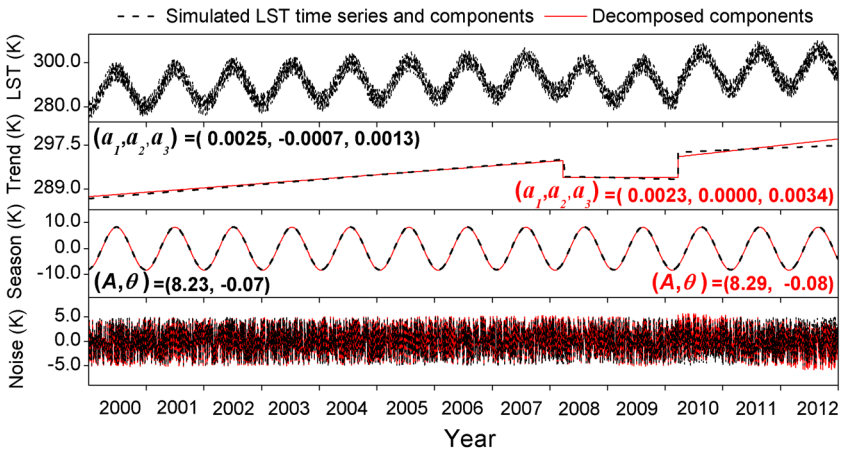

Figure 4. An example of the time series simulation and decomposition. (a_i, A, θ) in black and red are the (trend slope of subperiod i, seasonal amplitude, phase shift) of the simulated and decomposed components, respectively.

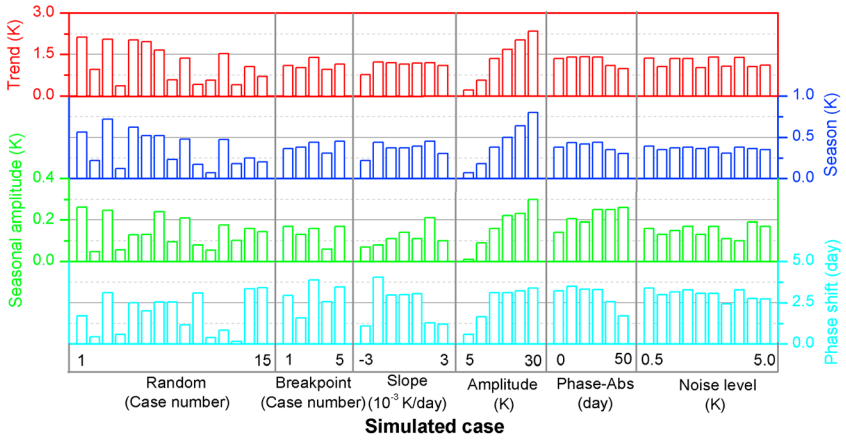

Figure 5. Decomposition errors of various simulated cases (Table 1). The first and second lines show the root-mean-square errors (RMSEs) between the decomposed and simulated trend and seasonal components, respectively. The third and fourth lines show the absolute differences (ADs) between the derived and simulated seasonal amplitudes and phase shifts, respectively. Phase-Abs denotes the absolute value of the phase shift.

the AD rather than the RMSE is an appropriate measure between two values. However, the RMSE is more desirable than mean AD as a difference measure of two sets of values (i.e., the decomposed and simulated trend/seasonal components) when the objective is to reveal model performance under various conditions [*Chai and Draxler*, 2014].

For the 15 random cases (the first column in Figure 5), the average RMSEs of trend and seasonal components and ADs of seasonal amplitudes and phase shifts are 1.18 K, 0.36 K, 0.14 K, and 2.0 days, respectively, ranging from 0.36 to 2.12 K, 0.07 to 0.72 K, 0.05 to 0.26 K, and 0.0 to 4.0 days, respectively. Figure 5 demonstrates that the breakpoint position, trend slope, phase shift, and noise level have little influence on the estimation of the trend and seasonal components. The average RMSEs of trend and seasonal components and ADs of seasonal amplitudes and phase shifts are 1.19 K, 0.38 K, 0.16 K, and 3.0 days, respectively. However, the errors almost linearly increase with the increasing seasonal amplitude. In particular, the RMSE of trend component is in the range of 0.21–2.34 K. This result may be because the large seasonal amplitude obscures the trend, making it difficult to accurately detect the relatively slight trend from the seasonal trend time series. This sensitivity illustrates that the trend decomposition must be carefully examined when the seasonal amplitude is rather large (e.g., over a desert area). In this study area, the seasonal amplitude is no more than 18.00 K (section 5.2), corresponding to RMSEs of 1.55 K and 0.45 K in the trend and seasonal components and ADs of 0.20 K and 3.0 days in the seasonal amplitude and phase shift.

4.2. With Various Timescales and Distributions of Missing Data

To analyze the impact of temporal resolution, time series with multiple timescales, including 1, 2, 4, 8, 16, 32, and 365 day and 13 year averaged monthly composite, were simulated, where the 1 day time series were generated using the basic values in Table 1 and the others were temporally aggregated from the 1 day data set. Figure 6 (the first column) shows that the largest errors appear in the 365 day composite and 13 year

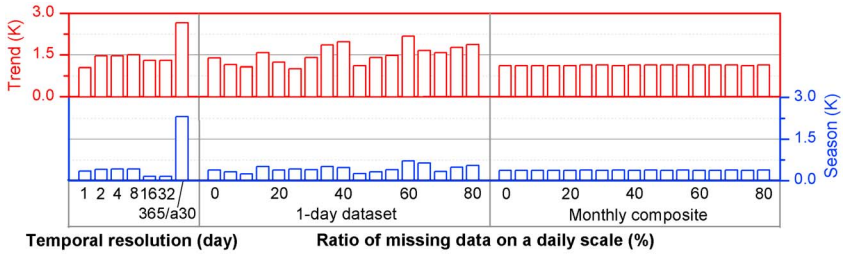

Figure 6. RMSEs between the decomposed and simulated trend and seasonal components at different temporal resolutions and ratios of missing data on a daily scale. a30 represents the 13 year averaged monthly composite.

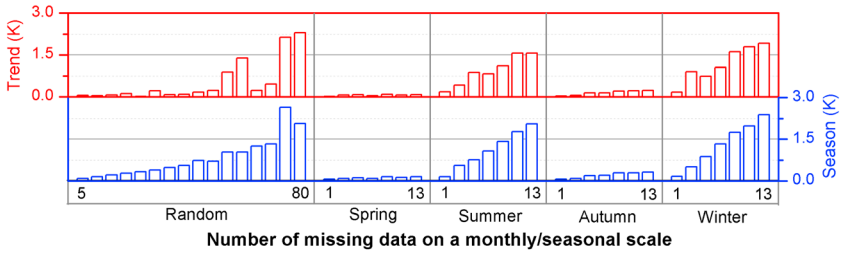

Figure 7. RMSEs between the decomposed and simulated trend and seasonal components under different numbers of missing data on a monthly/seasonal scale.

averaged monthly composite. This is because the breakpoint is difficult to accurately detect using the small-length time series [*Thanasis et al*., 2011; *Forkel et al*., 2013] and the trend is neglected in the 13 year averaged monthly composite. The errors of the 16 day and 32 day composites are the lowest because of the lower noise levels.

Furthermore, to explore the impact of missing data on a daily scale, we randomly removed 5% to 80% (with a step of 5%) of the daily values and then averaged the rest of the daily values to form the monthly data set. The errors before and after monthly aggregation are shown in Figure 6 (the second and third columns). It further reveals that the monthly composite is rather stable in coping with the missing data on a daily scale compared to the 1 day time series.

Considering that actual remotely sensed LSTs are sometimes missing due to clouds, heavy aerosols, system errors, etc. over a whole month or even season [*Zhou et al*., 2011], we further simulated cases with missing data on a monthly scale by two approaches: (1) randomly removing 5 to 80 (i.e., 3.2% to 51.3%) monthly values at a step of 5 and (2) removing seasonally concentrated values in randomly selected 1 to 13 years (with a step of 2).

In the random cases (the first column in Figure 7), the RMSEs of trend and seasonal components generally increase with the number of missing monthly data. The summer and winter cases (the third and fifth columns in Figure 7) exhibit more significant growing patterns of errors. This is because the loss of peaks/valleys in the LST time series leads to an underestimation/overestimation of the trend and an underestimation of the seasonal amplitude to achieve the smallest fitting errors. And this impact intensifies with increasing missing peaks/valleys. Moreover, breakpoints were falsely detected in some random (55, 60, 75, and 80), summer (11), and winter (9, 11, and 13) cases. In the random cases, the detected breakpoints are at the positions of numbers of concentrated missing data. Those in the summer/winter cases correspond to the valid summer/winter seasons whose forward or backward summer/winter seasons continuously have missing values. This method, however, is highly robust against the missing data in spring and autumn, with stable errors.

5. Application to MODIS/LST Time Series

Monthly averages were obtained from the daily Terra/Night MODIS/LSTs and then decomposed using TSDM, considering the lower noise level and smaller influence of the missing data according to the previous model analysis. We calculated RMSEs between the combination of the decomposed trend and seasonal components and the actual MODIS/LST time series to assess the fitting errors. Statistics of the RMSEs according to the land cover type and the number of missing monthly data are shown in Figure 8.

Figure 8a shows that the average RMSE over the study area is 1.62 K, with a standard deviation of 0.17 K, illustrating a good approximation of the original time series. The water bodies yield the highest errors (2.31 ± 0.32 K), while the croplands and the built-up lands have the lowest ones (1.45 ± 0.09 K and 1.48 ± 0.08 K, respectively). An increase in the RMSE with the number of missing monthly data was also observed in Figure 8b, which explained the order of error among the six land cover types: the water bodies had the largest number of missing data on a monthly scale (up to 18, i.e., 12%), mainly caused by the false alarm of the MODIS cloud mask due to snow [*Wang et al*., 2008], while the croplands and the built-up lands had the smallest numbers (up to 4, i.e., 3%). In the following sections, statistics of the decomposed trend and seasonal components were determined based on land cover type for an indirect evaluation, where the water bodies were not included due to their large fitting errors.

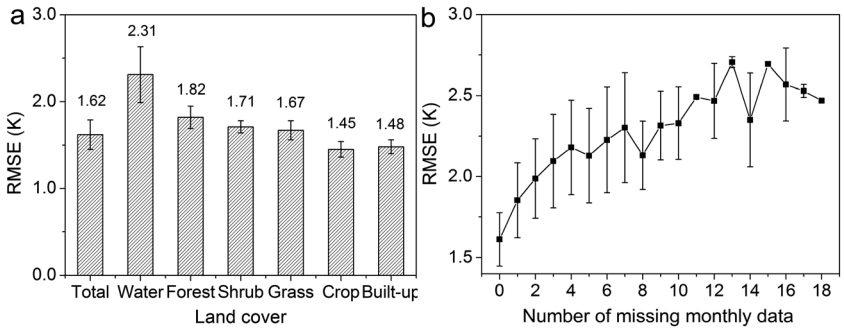

Figure 8. Statistics of the RMSEs between the combination of the decomposed trend and seasonal components and the actual MODIS/LST time series according to (a) the land cover type and (b) the number of missing monthly data.

5.1. Trend Component

Zero, one, and two breakpoints were detected over 30 432 (95.0%), 1505 (4.7%), and 103 (0.3%) pixels, respectively. The breakpoints were determined using the OLS-MOSUM test on structural changes ($p < 0.05$) (section 2.1.2). Therefore, their trends were considered statistically significant. Yet, a significance test on the LST trend without a breakpoint was conducted using the method proposed by *Santer et al.* [2000] (see Text S2 for detail). Only those pixels with $p < 0.1$ (i.e., 53% of the study area, see Table S1) were then statistically analyzed by land cover (Table 2). A further significance test of trend differences among land covers [*Santer et al.*, 2000] (Text S3 and Table S2) indicated that forest, shrublands, and croplands had insignificant trend differences ($p > 0.1$). Therefore, they were combined for statistics of trend slope and average (Table 2). Their trends were different ($p < 0.1$) from the trends over grasslands and built-up lands, which were meanwhile different from each other ($p < 0.1$).

Table 2 shows that the mean trend slope over 53% of the study area without a breakpoint ($p < 0.1$) was −0.086 K/yr with a standard deviation of 0.025 K/yr. This indicates a gradual decreasing trend during 2000–2012 of approximately −1.12 K (namely, the nighttime LST was becoming colder). Among the five land cover types (Table 2), the urban and built-up lands exhibited the smallest rate of change (−0.051 ± 0.056 K/yr). This might be attributed to the urban anthropogenic heat flux [*Yang et al.*, 2014] that elevated LST [*Hu et al.*, 2012] and thus decelerated the decrease of nighttime LST. The forest, shrublands, and croplands had a medium-level trend slope of −0.073 ± 0.025 K/yr, while the grasslands showed the strongest change (−0.101 ± 0.019 K/yr).

Table 2 also reveals that the urban and built-up lands had the highest average value of trend components. Urban canyon geometry, building materials, vegetation, and anthropogenic heat have been documented to be the primary factors in the urban energy balance [*Oke*, 1982, 1988; *Oke et al.*, 1991]. Canyon geometry reduces the effective albedo and sky view factor, increasing the multiple reflection of short-wave radiation between surfaces and decreasing long-wave radiation loss to the sky. This results in great heat storage within the canyon structure [*Oke*, 1982; *Goward*, 1981; *Rizwan et al.*, 2008]. Typical building materials and reduction in evaporating surfaces in urban areas also contribute to increasing sensible heat flux and reducing latent heat flux [*Carlson et al.*, 1981; *Oke*, 1988; *Rizwan et al.*, 2008]. Anthropogenic heat release mainly from transportation, building, and residential sectors is another primary heat source [*Grimmond*, 1992; *Sailor and Lu*, 2004; *Christen and Vogt*, 2004]. These factors all together lead to quantities of heat emittance at night [*Carlson et al.*, 1981; *Tiangco et al.*, 2008], yielding higher urban temperatures.

Table 2. Statistics of the Slope and Average of the Trend Component by Land Cover Over Pixels Without a Breakpoint[a]

	Slope (K/yr)				Average (K)			
	Min	Max	Mean	SD	Min	Max	Mean	SD
Total	−0.314	0.140	−0.086	0.025	269.08	284.48	278.04	2.12
FSC	−0.246	−0.104	−0.073	0.025	273.21	282.42	279.25	1.14
Grass	−0.224	0.108	−0.101	0.019	269.78	281.45	275.13	1.53
Built-up	−0.162	0.140	−0.051	0.056	272.61	284.48	280.48	1.77

[a]All of the trends and trend differences among land covers are significant at the 0.1 level or better. FSC: combination of forest, shrublands, and croplands.

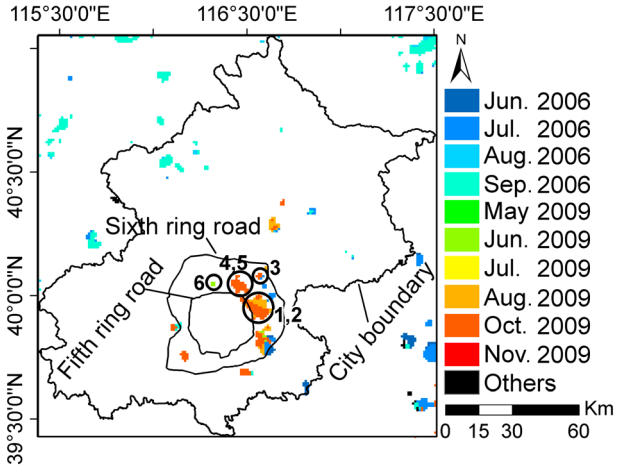

Figure 9. Spatial pattern of the timing of the detected breakpoints. Black circles mark the examples of areas with considerable land cover change during the time when breakpoints appeared.

The spatial pattern of the timing of the detected breakpoints is displayed in Figure 9. It shows that 33.4% of the breakpoints occurred in 2009, mostly located between the fifth and sixth ring roads, particularly in the northeast area. Their mean trend slopes were 0.084 K/yr during 2000–2009 and 0.245 K/yr during 2009–2012, demonstrating an accelerated increase after 2009. Meanwhile, 62.8% of the breakpoints were in 2006, mostly located in the grasslands and croplands outside of the Beijing city boundary (i.e., in Hebei province). Their mean trend slopes were −0.105 K/yr during 2000–2006 and −0.387 K/yr during 2006–2012.

To explore the reasons for the abrupt changes in LST time series, a number of high-resolution images during 2000–2012 were collected from Google Earth (copyright at Google Company). Figure 10 shows an example of areas with breakpoints. A large-scale house demolition was conducted during 2009–2010, and vegetation was later planted over the demolished area. The land cover change from the built-up surface to the bare soil surface during 2009–2010 corresponded to the LST breakpoints in October 2009. Five other examples marked in Figure 9 are shown in Text S4 and Figures S1–S5. These examples illustrate

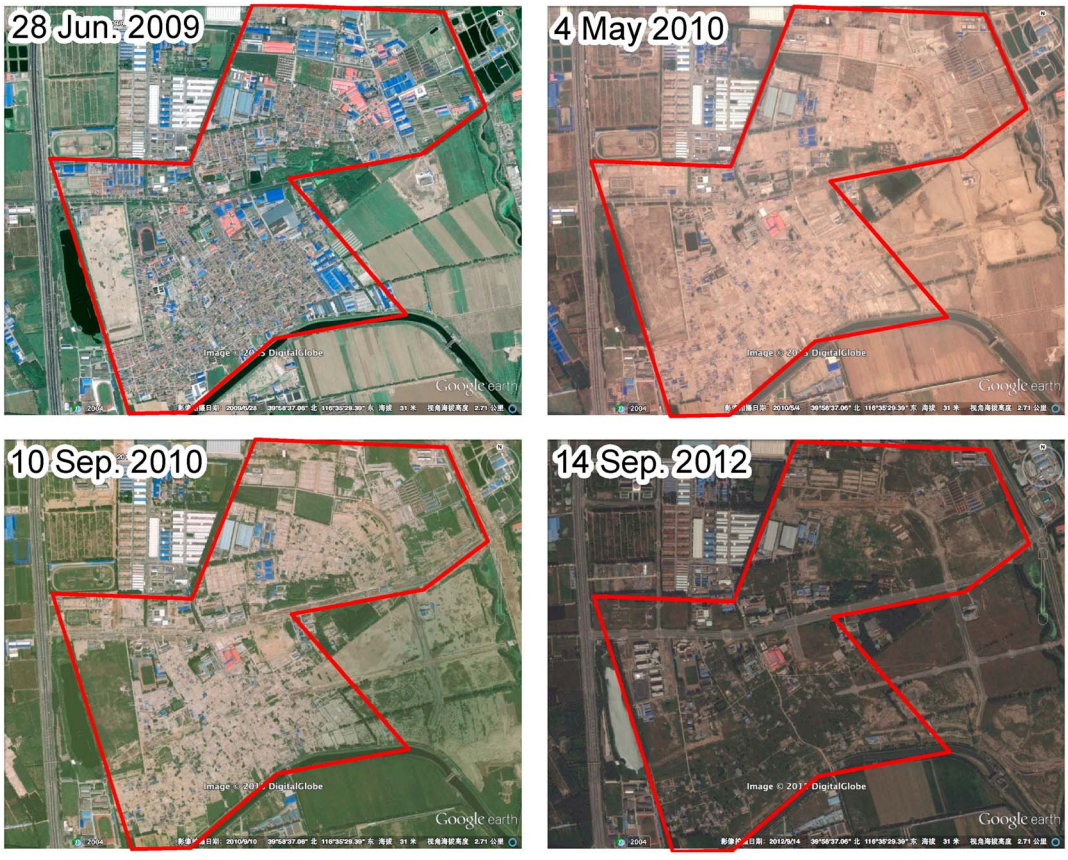

Figure 10. True color images (3.2×2.5 km^2) obtained from Google Earth at example 1 (Figure 9): near High School Attached to Northeast Normal University, Chaoyang District, Beijing.

Table 3. Statistics of the Seasonal Amplitude and the Phase Shift by Land Cover[a]

	Seasonal Amplitude (K)				Phase Shift (day)			
	Min	Max	Mean	SD	Min	Max	Mean	SD
Total	12.53	17.53	15.51	0.73	−42.5	−21.4	−26.8	1.4
Forest	12.80	16.23	14.65	0.59	−39.1	−24.6	−27.9	1.2
Shrub	13.51	15.82	14.62	0.45	−28.0	−25.1	−26.8	0.6
Grass	13.45	17.05	15.83	0.43	−31.7	−24.2	−27.4	1.0
Crop	13.94	17.00	16.02	0.37	−31.5	−23.3	−26.0	1.1
Built-up	14.35	16.98	15.74	0.40	−31.1	−23.7	−25.7	0.8

[a]Differences in mean/standard deviation among land covers are significant at the 0.001 level, except for the means of seasonal amplitude between the forest and shrublands.

that the breakpoints detected by TSDM appeared with considerable interannual land cover changes (e.g., vegetation ↔ buildings ↔ bare soil). However, due to the low frequency of the Google Earth images, it is difficult to match them precisely in time.

5.2. Seasonal Component

Pearson's r between the seasonal component and the detrended LST time series was 0.99, showing a good approximation of the seasonal fluctuation. Table 3 shows the statistics of the seasonal amplitude and phase shift by land cover. Independent-samples t test and F test (Text S5) showed that the seasonal amplitudes/phase shifts were different ($p < 0.001$) among land covers in both mean and variance perspectives, except that the forest and shrublands had insignificant differences in the average of seasonal amplitude.

The average seasonal amplitude was 15.51 K, with a standard deviation of 0.73 K (Table 3). The forest and shrublands showed smaller seasonal amplitudes (14.65 ± 0.59 K and 14.62 ± 0.45 K, respectively) than the croplands (16.02 ± 0.37 K). This indicated that the croplands intensified the seasonal temperature oscillation around trend, which was probably related to the crop phenology (section 6.3). The average phase shift was −26.8 days, with a standard deviation of 1.4 days (Table 3), indicating that the lowest and highest LSTs appeared around 16 January and 16 July. The forest had the largest absolute value of phase shift, while the urban and built-up lands showed the smallest one. It illustrates that the forest had a large thermal lag (i.e., high heat capacity and low conductivity) to delay temperature increase, while the urban and built-up lands quickly responded to the heating up [*Weng and Fu*, 2014]. Furthermore, the largest standard deviations of the seasonal amplitudes and phase shifts were both found in forest (Table 3). It was attributed to the varied vegetation species, abundance, growing status [*Weng and Fu*, 2014], and elevations.

Compared with the seasonal parameters retrieved from other satellite data, e.g., the Landsat Thematic Mapper (TM)/LSTs used by *Weng and Fu* [2014], our results exhibited smaller differences among land covers. Besides the regional differences, the lower spatial resolution (1 km) and the utilization of nighttime LSTs could be the probable causes.

6. SUHII and Correlation Analysis

6.1. Trend and Seasonal Patterns of SUHII

A significance test of trend differences (Table S2) between urban (i.e., built-up lands) and rural (i.e., croplands) temperatures revealed that the rural areas had a decreasing trend slope stronger ($p < 0.05$) than the urban areas (Table 2). This resulted in an increasing trend in SUHII from 1.87 to 2.16 K during 2000–2012 (0.022 ± 0.006 K/yr, $p < 0.05$). Furthermore, SUHII presented a concave seasonal curve at night with the minimum in summer and the maximum in winter.

6.2. Correlation Analysis of the LST and SUHII Trends

First, we compared the breakpoints of LST with the breakpoints of NDVI and white-sky albedo (WSA) to supplement the visual analysis in section 5.1. We found that the NDVI and WSA breakpoints matched 175 and 149 of the LST breakpoints (13% and 11%), respectively, and 304 LST breakpoints (22%), together, which were mostly located between the fifth and sixth ring roads (Figure 9). It not only reveals that the abrupt change in land surface properties could cause the breaks in the LST trend but also implies that other factors should also be taken into account. Therefore, we further investigated the co-occurrence of

Table 4. Stepwise Linear Regression-Derived Explanation (%) of Each Factor on the LST and SUHII Trends During 2000–2012[a]

	(△) NDVI	(△) WSA	(△) AT	(△) DATR	(△) RF	(△) RHU	(△) WIN	(△) SSD	Total
Mountainous	0	0	+26	−39	0	0	−21	0	86
Rural	0	0	+34	+19	0	+19	0	0	72
Urban	−8	−14	+10	+5	0	0	0	0	37
SUHII	+36	0	0	0	+39	0	0	0	75

[a]All of the correlations are significant at the 0.05 level, and the sign indicates positive or negative correlation. NDVI: normalized difference vegetation index; WSA: white-sky albedo; AT: air temperature; DATR: diurnal air temperature range; RF: total rainfall; RHU: relative humidity; WIN: wind speed; SSD: sunshine duration.

LST breakpoints with the breakpoints of the meteorological variables. The results indicated no match with air temperature (AT), diurnal air temperature range (DATR), total rainfall (RF), relative humidity (RHU), wind speed (WIN), and sunshine duration (SSD). However, due to the lack of wide coverage of meteorological data, this analysis is hardly conclusive. The abrupt change in human activity or anthropogenic heat is another probable contributor and should be included in future studies. One may consider that the occurrence of large fire on vegetated areas could cause the breaks in the LST time series due to the permanent/long-term change from vegetation to bare land. However, such correspondence was not observed because the burned area of fire events did not exceed 1 km^2 over this study area since 2000 according to the records by the National Forest Fire Prevention Headquarters Office (http://www.slfh.gov.cn/slfhw/default.aspx).

Second, Table 4 shows that different factors were responsible for the LST trends in different areas. For the urban area, WSA, AT, and NDVI made primary contributions of 14%, 10%, and 8%, respectively. The correlations of WSA and NDVI were both negative, which is reasonable considering the heat reduction effects of vegetation and high reflectance surfaces [*Mackey et al*., 2012; *Quan et al*., 2014a]. Although previous studies have demonstrated that NDVI is little related to the nighttime temperatures due to the absence of evaporative cooling [*Arnfield*, 2003; *Peng et al*., 2012], they focused on the spatial correlation. Our study paid attention to the long-term LST variation, and the growing vegetation cover could gradually reduce the nighttime LST due to the reduced amount of stored heat energy during the day [*Tiangco et al*., 2008].

For the rural area, AT, DATR, and RF were the main contributors (34%, 19%, and 19%, respectively), while for the mountainous area, DATR, AT, and WIN had the prevailing impacts (39%, 26%, and 21%, respectively). AT showed a considerably positive contribution over all of the three areas because of the close surface-air interaction at night [*Nichol*, 2005]. RF played a significant role (negative) over the rural area rather than over the urban area. It may be attributed to their greatly different responses to rainfall: rural surfaces tend to absorb and store rain to increase soil water content and to use it for evapotranspiration, while the rainfall is mostly resisted by urban impervious surfaces and piped out by a city drainage system. The total explanatory power over the urban, rural, and mountainous areas was 37%, 72%, and 86%, respectively. It implies that the land surface and climate change are generally sufficient to explain the trends over rural and mountainous areas, while other factors (e.g., anthropogenic heat flux) are also responsible for the urban LST trend.

Finally, △RF and △WSA were found to be the primary driving factors of the SUHII trend: 39% (positive) and 36% (negative), respectively (Table 4). As mentioned above, RF was the prevailing contributor (negative) of the LST trend in the rural area but not in the urban area, which indirectly caused the urban-rural difference of LST. WSA is a negative indicator for solar heat absorption [*Peng et al*., 2012]. Therefore, the decreasing trend in △WSA (negative value), i.e., the increasing urban-rural difference of WSA, intensified the urban-rural differences in heat absorption and storage during the day. This in turn increased the SUHII at night [*Zhou et al*., 2014]. Although the contribution of △RF is larger, increasing urban albedo with respect to the rural albedo is a more practical way of reducing SUHII.

Among many mitigation strategies, the albedo and vegetation strategies (e.g., reflective roofs, green roofs, street trees, and parks) have gained the most acceptance and been practically implemented in some cities [*Rizwan et al*., 2008; *Mackey et al*., 2012]. This correlation indicates that the albedo strategy produces larger cooling than the vegetation strategy from the long-term perspective on a city scale [*Mackey et al*., 2012;

Table 5. Stepwise Linear Regression-Derived Explanations (%) of 13 Year Averaged NDVI and WSA on the Seasonal Amplitude and Phase Shift of LST as Well as Those of the Difference Variables on the Seasonal SUHII During 2000–2012[a]

	(△) NDVI	(△) WSA	△AT	△DATR	△RF	△RHU	△WIN	△SSD	Total
Amplitude	−2	+54							56
Phase	−1	+8							9
SUHII	+24	0	0	0	0	+9	+9	0	42

[a]All of the correlations are significant at the 0.05 level, and the sign indicates positive or negative correlation.

Zhaoet al., 2014]. This, however, does not suggest that the albedo strategy is more appropriate. The reasons are twofold.

1. Increasing urban albedo would induce urban cooling in both summer and winter [*Zhou et al*., 2014], which would deteriorate residential comfort and aggravate the energy consumption by heating facilities in winter. Vegetation has a significant cooling effect only in summer but not in winter due to phenology [*Quan et al*., 2014a]. This is conducive to reducing SUHII in summer while maintaining the higher urban temperatures during winter nighttime.
2. Vegetation possesses great ecosystem service values [*Bolund and Hunhammar*, 1999] that reflective roofs cannot match. However, to generate a widespread cooling effect, the vegetation must be dense enough [*Mackey et al*., 2012]. It requires sufficient amounts of installation and maintenance support, particularly water support, which would be a challenge in cities with a water shortage issue [*Mcdonald et al*., 2011], e.g., in Beijing.

6.3. Correlation Analysis of the Seasonal Amplitude, Phase Shift, and Seasonal SUHII Pattern

First, as presented in Table 5, white-sky albedo (WSA) is the primary factor (54%, positive) affecting the seasonal amplitude spatially, which explains the relativities of seasonal amplitudes among land covers shown in Table 3. However, larger albedo, assuming albedo is annually unchanged, would correspond to a smaller seasonal amplitude of solar heat absorption, which is often considered to produce a smaller seasonal amplitude of LST during nighttime. This is in contrast to the positive correlation found in Table 5. There may be two aspects.

1. The thermal properties are the primary determinant underlying WSA. Generally, a larger WSA coexists with a smaller thermal capacity and inertia [*Wang et al*., 2005] and sensitively responds to the seasonal heating up and cooling down, consequently causing a larger seasonal amplitude.
2. The seasonal variation of albedo [*Wang et al*., 2005] was ignored. The summer-winter difference of WSA was positive over forest but negative over croplands. Compared to the heat absorption with the averaged WSA, the summer-winter difference of heat absorption over forest was weakened, while that over croplands was enlarged, which further affected their seasonal amplitudes. Therefore, the seasonal variations of the driving factors should be considered in future studies of seasonal parameters.

Regarding the phase shift, NDVI and WSA, in total, only explained 9% (1% and 8%, respectively) of its spatial variation. This implies that a more complex pattern in the phase shift exists than that in the seasonal amplitude. Including other biophysical variables, e.g., normalized difference water index (NDWI), may not notably increase the explanatory power over NDVI and WSA because the multiyear averaged NDWI and NDVI are linearly correlated [*Jackson et al*., 2004].

Second, due to the crop phenology, the urban-rural difference in NDVI was larger in summer and smaller in winter, forming a concave seasonal curve of △NDVI (negative) and consequently a positive correlation (24%) with the seasonal pattern of the nighttime SUHII (Table 5). This correlation actually reflects a contribution by temperature cooling rate. The thermal inertia of the urban interface was generally larger than that of the rural interface primarily due to the urban canyon structure [*Goward*, 1981; *Kusaka and Kimura*, 2004]. However, in July and August when crops were luxuriant and irrigation was adequate, the proportion of latent heat flux grew [*Peng et al*., 2012] due to strong evapotranspiration [*Wang et al*., 2006]. This indicated that the rural temperature cooling rate was smaller than the urban one in July and August. Even so, the urban LSTs were higher than the rural LSTs at night because the daytime solar heating of croplands was much smaller considering the evapotranspiration [*Carlson et al*., 1981]. In the other months, the rural temperature cooling was faster than

the urban one, and their difference was gradually enlarged with dry winter coming. Consequently, the urban-rural difference of LST at night was reduced in July and August but enhanced in winter.

A similar explanation also applies to the daytime SUHII. The rural temperature heating rate is smaller than the urban one in July and August, enlarging SUHII, whereas the rural heating is faster than the urban heating in the other months, narrowing SUHII. Therefore, a convex seasonal variation is formed in SUHII during the day [*Tran et al*., 2006; *Wang et al*., 2007; *Imhoff et al*., 2010]. One special case is that urban cool island appears in the day if rural heating rate is remarkably larger than the urban one [Goward, 1981]. Yet, other factors (e.g., aerosols) also contribute to urban cool island formation [*Wang et al*., 2007].

A negative correlation (−45%) was found using univariate linear regression between the seasonal variations of $\triangle$DATR (diurnal air temperature range) and nighttime SUHII. It is reasonable given the thermal inertia and the positive correlation between diurnal surface and air temperature ranges [*Peng et al*., 2012]. However, the stepwise regression analysis (Table 5) showed 0% of explanation by $\triangle$DATR. It might be because $\triangle$NDVI already included this underlying mechanism.

Third, $\triangle$RHU (relative humidity) and $\triangle$WIN (wind speed) were the other two contributors (Table 5). In Beijing, $\triangle$RHU was positive in winter [*Lee*, 1991] because of urban continuous evapotranspiration, anthropogenic heat emission (e.g., transportation), or/and rural dewfall [*Holmer and Eliasson*, 1999]. However, it was negative in summer mainly due to the large evapotranspiration in the rural area [*Unkašević et al*., 2001; *Liu et al*., 2009]. $\triangle$RHU generated a positive correlation (9%) because an increasing urban-rural difference in RHU corresponded to a larger difference in the power of preventing the surface heat dissipation [*Zhao et al*., 2014]. In contrast, some studies illustrate a negative correlation, regarding the proportion between the latent and sensible heat flux [*Kim and Baik*, 2002; *Zhou et al*., 2011]. Nevertheless, these studies did not include the urban-rural difference, the temporal variation of $\triangle$RHU [Holmer and Eliasson, 1999], and, most importantly, the weak nighttime latent flux.

Previously, WIN was documented to be negatively related to urban heat island because the advection and turbulent activity are enhanced as the wind speed increases [*Holmer and Eliasson*, 1999; *Kim and Baik*, 2002]. However, the previous studies did not include the urban-rural difference in wind speed, which, in Beijing, generally showed a concave seasonal variation with a valley in summer and a peak in winter/spring. This variation of $\triangle$WIN exhibited a positive correlation with the nighttime SUHII (9%). This is because the larger urban-rural difference in wind speed enhanced the heat transfer between the urban and rural areas and finally decreased SUHII to some extent. However, $\triangle$RHU and $\triangle$WIN did not play crucial roles in the seasonal variation of SUHII.

Fourth, some studies suggest that the larger nighttime SUHII in winter is probably caused by the pronounced urban-rural difference in albedo [*Zhou et al*., 2014]. However, it does not necessarily indicate a larger urban-rural difference in heat storage because solar radiation decreases in winter. Moreover, the summertime and wintertime $\triangle$WSA were both negative in Beijing primarily due to urban canyon geometry [*Oke*, 1982], and the summer-winter difference of $\triangle$WSA was also negative (namely, summer $|\triangle\text{WSA}| >$ winter $|\triangle\text{WSA}|$). This revealed that the seasonal variation of $\triangle$WSA had little direct correlation with the seasonal pattern of SUHII (0% in Table 5). Nevertheless, $\triangle$WSA-induced urban-rural difference in the seasonal amplitude (combining Tables 3 and 5) could account for the concave seasonal pattern of SUHII.

Finally, considering that anthropogenic heat flux composes a large portion of the total energy release at night [*Arnfield*, 2003; *Peng et al*., 2012], several studies suggest that large amounts of urban anthropogenic heat release during wintertime may indirectly strengthen the nighttime SUHII [*Zhou et al*., 2014]. It may increase the total contribution in Table 5 (42%). However, this conjecture must be studied quantitatively in the future by including the urban-rural difference of anthropogenic heat flux and its seasonal variation [*Rizwan et al*., 2008] while including other variables.

7. Uncertainty Analysis

7.1. Systematic Errors

One may be concerned that the trend may be caused by systematic errors, particularly the aging thermal sensor and the drift in the overpass time over years. First, the change in MODIS response for thermal bands can be taken into account by scheduled on-orbit calibration using an onboard blackbody [*Xiong et al*., 2014],

whose temperature has exhibited excellent long-term stability since 2000: the drift was less than 0.04 K over 14 years [*Xiong et al*., 2014].

Second, a linear trend with a slope of −0.7 min/yr and a standard deviation of 0.2 min/yr was found in the overpass time of Terra/MODIS in this study ($p < 0.05$), indicating an advance of overpass time about 9 min at night (~22:00) during 2000–2012. Thus, a gradual increase in LST was expected: a maximum of 0.15 K (0.012 K/yr) according to the diurnal temperature cycles of different surface components [*Quan et al*., 2014b]. Consequently, the estimated trend in section 5.1 should be further strengthened from −0.086 K/yr up to −0.098 K/yr after excluding the deviation caused by this drift.

7.2. LST Retrieval Errors

MODIS/LST accuracy has been reported over most homogeneous surfaces [*Wan*, 2014]. Yet, the accuracy over heterogeneous surfaces remains unclear to date [*Liu et al*., 2006; *Li et al*., 2013]. This is because surface heterogeneity causes a complex mixture of components with varied temperatures and emissivity in one pixel and leads to a strong variation of LST in space, time, and angle [*Prata et al*., 1995; *Pinheiro et al*., 2006]. Consequently, the ground-based validation of satellite-derived LST over heterogeneous surfaces suffers from great challenges [*Quan et al*., 2014b]. Even though upscaling methods have been proposed to generate pixel-scale temperatures from in situ measured surface temperatures [*Guillevic et al*., 2012, 2013; *Ermida et al*., 2014], accurate emissivity and fractions of the main surface covers are required and yet difficult to estimate. Moreover, the uncertainty during the upscaling and georegistration obscures the validation [*Wan*, 1999; *Quan et al*., 2014b].

Therefore, we, here, theoretically estimated uncertainties during LST retrieval. Emissivity, atmospheric condition, and angular effects are reported as the main factors [*Mitraka et al*., 2012], where the impacts of the latter two are rather small at night [*Wan and Li*, 2008] and, thus, were not discussed in this study. It is reported that an uncertainty in emissivity of 1% may cause an LST error of about 0.3–3.0 K with different atmospheric conditions, view angles, land covers, retrieval algorithms, etc. [*Becker*, 1987; *Wan and Dozier*, 1996; *Ottle and Stoll*, 1993; *Jiménez-Muñoz and Sobrino*, 2003; *Wan and Li*, 2008; *Li et al*., 2013]. To achieve a 1 K accuracy of LST, uncertainty of emissivity under 0.01 is essential.

MOD11A1 in version 5 is retrieved from a generalized split-window algorithm with classification-based emissivity estimation [*Wan and Dozier*, 1996; *Snyder et al*., 1998]. This estimation obtains a sufficient accuracy (~0.01) of emissivity over 70% of natural land surfaces, thus satisfying the goal of 1 K LST accuracy. However, soil moisture, vegetation phenology, snow, and ice, aside from classification errors, can degrade the emissivity accuracy [*Gillespie et al*., 1996; *Snyder et al*., 1998; *Li et al*., 2013]. Moreover, emissivity estimation over urban surfaces can be largely biased due to the significant intraclass variation [*Stathopoulou et al*., 2007], component mixing [*Mitraka et al*., 2012], and anisotropy [*Ren et al*., 2011].

According to *Stathopoulou et al*. [2004], an emissivity error of 0.01/0.02, corresponding to vegetation (emissivity: 0.98–0.99)/bare surface (emissivity: 0.96–0.98), yielded an LST error of about 0.5/1.0 K using the split-window algorithm under normal conditions. Consequently, the error of instantaneous SUHII caused by emissivity deviation can reach up to 1.5/2.0 K in summer/winter. Nonetheless, the model analysis (section 4.1) showed great robustness of TSDM against noise levels (0.0–5.0 K). This suggests that an LST error under 5.0 K hardly affects the decomposed trend and seasonal components of LST time series and further the temporal patterns of SUHII, which outperforms the intercomparison of sample images [*Coppin et al*., 2004].

Daily minimum near-surface air temperatures during 2000–2012 were collected from 15 Beijing weather stations (http://cdc.cma.gov.cn/home.do). Fifty percent of them showed decreasing trends ($p < 0.1$): an average of −0.105 K/yr with a standard deviation of 0.087 K/yr. It further supports that the decreasing trend of LST is a statistically significant biophysical phenomenon instead of an artifact of the observational conditions.

8. Future Issues

First, a long period of time series accounts for a more statistically significant temporal variation, and the prediction of future temperatures is more justified. However, larger uncertainties would be included, and breakpoints of the seasonal component may need to be considered. On the other hand, a small period of time series is often not useful for trend detection, and the summarization of temporal pattern can hardly be extended to show the future variation. The statistical probability is also problematic with the small number

of the data sets [*Forkel et al*., 2013]. In addition, the length of the period is related to the temporal resolution, the number of missing values, the site-specific climate change, the trend magnitude, the land cover change, etc., which should be further discussed.

Second, abrupt changes in thermal sensor or considerable drift in the overpass time can alter the detected trend component (including breakpoints) since TSDM has yet incorporated approaches for correcting these effects. Therefore, more caution is needed when data with these effects are used, e.g., advanced very high resolution radiometer/LSTs [*Price*, 1991]. Various approaches have been proposed to reduce these influences [*Gutman*, 1999; *Gleason et al*., 2002; *Pinheiro et al*., 2004; *Sobrino et al*., 2008; *Julien and Sobrino*, 2012] and only the corrected LST time series can then be adopted in TSDM.

Third, because solar radiation enhances the instability of the atmospheric boundary, the probability for clouds to form during the day is higher than during nighttime, particularly over urban areas in summer and winter due to significant sensible heat flux, air turbulence, convergence, precipitation, and heavy aerosols [*Wang et al*., 2008; *Zhou et al*., 2011; *Hu and Brunsell*, 2013; *Quan et al*., 2014a]. For LSTs with lower temporal resolutions (e.g., Landsat TM/LST with a temporal resolution of 16 days), the probability of obtaining missing values on a monthly scale is further increased. Therefore, the satellite-derived daytime LST time series may suffer from vast numbers of missing monthly values, which could increase uncertainties in time series analysis [*Clinton and Gong*, 2013]. This highlights the necessity of improving the current model under a situation of concentrated missing data.

Fourth, the decomposed components vary with the acquisition time due to the diurnal temperature variation. However, temporal patterns, relative orders of parameter values among land cover types, and correlations with the driving factors presented in this study remain applicable at other nighttimes, considering thermal stability at night [*Zhou et al*., 2013]. The daytime LSTs, in contrast, may have different or even converse patterns from the nighttime ones. For example, the urban seasonal amplitude is probably larger than the rural one over Beijing during the day, forming a convex seasonal variation of SUHII during the day (section 6.3). Application of TSDM to four-time MODIS/LSTs per day is able to determine the changes at different times. Furthermore, hourly application to a long-term geostationary data set may be able to explore the diurnal patterns of the trend and seasonal parameters and further to construct long-term full time series.

Finally, surface energy and radiation budget is essential for the formation of thermal environment [*Quattrochi and Luvall*, 2009; *Luvall et al*., 2015; *Lo et al*., 1997]. The partitioning of net radiation (and the possible anthropogenic heat flux) into sensible, latent, and soil heat flux controls temperature heating and cooling and finally forms distinct patterns and dynamics of temperature. This thermal response can be characterized by thermal response number (TRN), the ratio of total net radiation to temperature change for a short term [*Luvall and Holbo*, 1989; *Quattrochi and Luvall*, 1999]. TRN is physically based, distinguishable among various surface types, and computable by remote sensing data and in situ radiation measurements [*Quattrochi and Luvall*, 2009; *Luvall et al*., 2015]. In the case of obtainable LST observations with a short time interval (~30 min) and a MODIS-like spatial scale (1 km) during several years, TRN can be calculated to quantify the thermal responses of different land covers and thus help better understand the trends and seasonal variations in LSTs and SUHIIs.

9. Conclusions

TSDM proposed in this study is a method to decompose remotely sensed LST time series into trend, seasonal, and noise components for simultaneously characterizing the long-term (including gradual and abrupt) and seasonal variations of LST. The trend component indicates long-term climate change and land development and management and is described as a piecewise linear function with iterative breakpoint detection. The seasonal component illustrates the annual change of insolation and is therefore modeled by a sinusoidal function on the detrended data.

Simulation analysis revealed that TSDM is robust against breakpoint, trend slope, phase shift, noise level, and missing daily data but is sensitive to the seasonal amplitude and missing data on a monthly scale. It suggests that this method may be less appropriate for areas with a large seasonal amplitude (e.g., over a desert area) and for daytime LST time series over urban areas. TSDM was further applied to Terra/Night MODIS/LST time series during 2000–2012 over Beijing. Results indicated an overall RMSE of 1.62 K between the combination of the decomposed trend and seasonal components and the actual MODIS/LST time series.

Generally, a decreasing trend of LST (~ −0.086 K/yr, $p < 0.1$) was detected over 53% of the study area, while an increasing trend with breakpoints in 2009 (~0.084 K/yr and ~ 0.245 K/yr before and after 2009, respectively) was found between the fifth and sixth ring roads. The breakpoints of NDVI and white-sky albedo (WSA) matched 22% of the LST breakpoints, while the breaks induced by other factors (e.g., anthropogenic heat) may attribute to the rest of LST breakpoints. The LST trends over urban, rural, and mountainous areas were primarily driven by different factors, i.e., WSA, AT (air temperature), and NDVI over urban areas; AT, DATR (diurnal air temperature range), and RF (rainfall) over rural areas; and DATR, AT, and WIN (wind speed) over mountainous areas. The decreasing trend was stronger over croplands than over urban and built-up lands ($p < 0.05$), resulting in an increasing trend in SUHII at night (0.022 ± 0.006 K/yr), which was mainly related to the trend of $\triangle$RF and $\triangle$WSA (39% and −36%, respectively).

Furthermore, the seasonal amplitude of LST was dominated by WSA (54%), which was controlled primarily by thermal properties and seasonal variation in albedo. The phase shift had a more complicated pattern. The nighttime SUHII exhibited a concave seasonal curve (minimum in summer and maximum in winter). This is primarily attributed to the seasonal variations of urban-rural differences in temperature cooling rate (related to canyon structure, vegetation, and soil moisture) and surface heat dissipation (affected by humidity and wind). Regarding the anthropogenic heat flux, the temporal variation in its urban-rural difference should be combined in future correlation analysis with SUHII.

TSDM can be extended to (1) long-term time series reconstruction of LST and LST-related surface or meteorological variables and (2) many other temperature-related fields, e.g., long-term climate change due to land cover change.

Acknowledgments

The MODIS data are available at NASA's Earth Observing System and Data and Information System (EOSDIS) (https://earthdata.nasa.gov/), the meteorological data are available at the China Meteorological Data Sharing Service System (http://cdc.cma.gov.cn/home.do), and the high-resolution images (Figures 10 and S1–S5) are available at Google Earth (copyright at Google Company). We thank Di Long with Tsinghua University for his help with improving the writing of this manuscript. This study was supported by grants from the National Natural Science Foundation of China (grant 41471348), National Key Basic Research Program of China (grant 2015CB954101), National Natural Science Foundation of China (grants 41301360 and 41421001), and Science and Technology Program of the Institute of Geographic Sciences and Natural Resources Research, CAS (grant Y5V5001MYE).

References

Arnfield, A. J. (2003), Two decades of urban climate research: A review of turbulence, exchanges of energy and water, and the urban heat island, *Int. J. Climatol.*, *23*(1), 1–26, doi:10.1002/joc.859.

Bai, J., and P. Perron (2003), Computation and analysis of multiple structural change models, *J. Appl. Econ.*, *18*, 1–22, doi:10.1002/jae.659.

Bechtel, B. (2012), Robustness of annual cycle parameters to characterize the urban thermal landscapes, *IEEE Geosci. Remote Sci. Lett.*, *9*(5), 876–880, doi:10.1109/LGRS.2012.2185034.

Beck, P. S. A., C. Atzberger, K. A. Høgda, B. Johansen, and A. K. Skidmore (2006), Improved monitoring of vegetation dynamics at very high latitudes: A new method using MODIS NDVI, *Remote Sens. Environ.*, *100*, 321–334, doi:10.1016/j.rse.2005.10.021.

Becker, F. (1987), The impact of spectral emissivity on the measurement of land surface temperature from a satellite, *Int. J. Remote Sens.*, *8*(10), 1509–1522, doi:10.1080/01431168708954793.

Bolund, P., and S. Hunhammar (1999), Ecosystem services in urban areas, *Ecol. Econ.*, *29*(2), 293–301, doi:10.1016/S0921-8009(99)00013-0.

Carlson, T. N., J. K. Dodd, S. G. Benjamin, and J. N. Cooper (1981), Satellite estimation of the surface energy balance, moisture availability and thermal inertia, *J. Appl. Meteorol.*, *20*(1), 67–87, doi:10.1175/1520-0450(1981)020<0067:SEOTSE>2.0.CO;2.

Chai, T., and R. R. Draxler (2014), Root mean square error (RMSE) or mean absolute error (MAE)?—Arguments against avoiding RMSE in the literature, *Geosci. Model Dev.*, *7*, 1247–1250, doi:10.5194/gmd-7-1247-2014.

Chen, X. L., H. M. Zhao, P. X. Li, and Z. Y. Yin (2006), Remote sensing image-based analysis of the relationship between urban heat island and land use/cover changes, *Remote Sens. Environ.*, *104*, 133–146, doi:10.1016/j.rse.2005.11.016.

Christen, A., and R. Vogt (2004), Energy and radiation balance of a central European city, *Int. J. Climatol.*, *24*(11), 1395–1421, doi:10.1002/joc.1074.

Cleveland, R. B., W. S. Cleveland, J. E. Mcrae, and I. Terpenning (1990), STL: A seasonal-trend decomposition procedure based on loess, *J. Off. Stat.*, *6*(1), 3–73.

Clinton, N., and P. Gong (2013), MODIS detected surface urban heat islands and sinks: Global locations and controls, *Remote Sens. Environ.*, *134*, 294–304, doi:10.1016/j.rse.2013.03.008.

Coppin, P., I. Jonckheere, K. Nackaerts, B. Muys, and E. Lambin (2004), Digital change detection methods in ecosystem monitoring: A review, *Int. J. Remote Sens.*, *25*(9), 1565–1596, doi:10.1080/0143116031000101675.

de Beurs, K. M., and G. M. Henebry (2005), A statistical framework for the analysis of long image time series, *Int. J. Remote Sens.*, *26*(8), 1551–1573, doi:10.1080/01431160512331326657.

Duan, S. B., Z. L. Li, B. H. Tang, H. Wu, and R. L. Tang (2014), Direct estimation of land-surface diurnal temperature cycle model parameters from MSG-SEVIRI brightness temperatures under clear sky conditions, *Remote Sens. Environ.*, *150*, 34–43, doi:10.1016/j.rse.2014.04.017.

Eliseev, A. V., and I. I. Mokhov (2003), Amplitude-phase characteristics of the annual cycle of surface air temperature in the northern hemisphere, *Adv. Atmos. Sci.*, *20*(1), 1–16, doi:10.1007/BF03342045.

Ermida, S. L., I. F. Trigo, C. C. DaCamara, F. M. Göttsche, F. S. Olesen, and G. Hulley (2014), Validation of remotely sensed surface temperature over an oak woodland landscape—The problem of viewing and illumination geometries, *Remote Sens. Environ.*, *148*, 16–27, doi:10.1016/j.rse.2014.03.016.

Forkel, M., N. Carvalhais, J. Verbesselt, M. Mahecha, C. Neigh, and M. Reichstein (2013), Trend change detection in NDVI time series: Effects of inter-annual variability and methodology, *Remote Sens.*, *5*(5), 2113–2144, doi:10.3390/rs5052113.

Galford, G. L., J. F. Mustard, J. Melillo, A. Gendrin, C. C. Cerri, and C. E. P. Cerri (2008), Wavelet analysis of MODIS time series to detect expansion and intensification of row-crop agriculture in Brazil, *Remote Sens. Environ.*, *112*, 576–587, doi:10.1016/j.rse.2007.05.017.

Gallo, K. P., and T. W. Owen (1998), Assessment of urban heat islands: A multi-sensor perspective for the Dallas-ft. Worth, USA region, *Geocarto Int.*, *13*(4), 35–41, doi:10.1080/10106049809354662.

Gillespie, A. R., S. Rokugawa, S. J. Hook, T. Matsunaga, and A. B. Kahle (1996), *Temperature/Emissivity Separation Algorithm Theoretical Basis Document, Version 2.4*, NASA/GSFC Greenbelt, Md.

Gleason, A. C. R., S. D. Prince, S. J. Goetz, and J. Small (2002), Effects of orbital drift on land surface temperature measured by AVHRR thermal sensors, *Remote Sens. Environ.*, *79*(2–3), 147–165, doi:10.1016/S0034-4257(01)00269-3.

Göttsche, F., and F. S. Olesen (2001), Modelling of diurnal cycles of brightness temperature extracted from METEOSAT data, *Remote Sens. Environ.*, *76*(3), 337–348, doi:10.1016/S0034-4257(00)00214-5.

Goward, S. N. (1981), Thermal behavior of urban landscapes and the urban heat island, *Phys. Geogr.*, *2*(1), 19–33, doi:10.1080/02723646.1981.10642202.

Grimmond, C. S. B. (1992), The suburban energy balance: Methodological considerations and results for a mid-latitude west coast city under winter and spring conditions, *Int. J. Climatol.*, *12*(5), 481–497, doi:10.1002/joc.3370120506.

Guillevic, P. C., J. L. Privette, B. Coudert, M. A. Palecki, J. Demarty, C. Ottlé, and J. A. Augustine (2012), Land surface temperature product validation using NOAA's surface climate observation networks—Scaling methodology for the Visible Infrared Imager Radiometer Suite (VIIRS), *Remote Sens. Environ.*, *124*, 282–298, doi:10.1016/j.rse.2012.05.004.

Guillevic, P. C., A. Bork-Unkelbach, F. M. Gottsche, G. Hulley, J. P. Gastellu-Etchegorry, F. S. Olesen, and J. L. Privette (2013), Directional viewing effects on satellite land surface temperature products over sparse vegetation canopies—A multisensor analysis, *IEEE Geosci. Remote Sens. Lett.*, *10*(6), 1464–1468, doi:10.1109/LGRS.2013.2260319.

Gutman, G. G. (1999), On the monitoring of land surface temperatures with the NOAA/AVHRR: Removing the effect of satellite orbit drift, *Int. J. Remote Sens.*, *20*(17), 3407–3413, doi:10.1080/014311699211435.

Halliday, S. J., A. J. Wade, R. A. Skeffington, C. Neal, B. Reynolds, P. Rowland, M. Neal, and D. Norris (2012), An analysis of long-term trends, seasonality and short-term dynamics in water quality data from Plynlimon, Wales, *Sci. Total Environ.*, *434*, 186–200, doi:10.1016/j.scitotenv.2011.10.052.

Holmer, B., and I. Eliasson (1999), Urban-rural vapour pressure differences and their role in the development of urban heat islands, *Int. J. Climatol.*, *19*(9), 989–1009, doi:10.1002/(SICI)1097-0088(199907)19:9<989::AID-JOC410>3.0.CO;2-1.

Hu, D., L. M. Yang, J. Zhou, and L. Deng (2012), Estimation of urban energy heat flux and anthropogenic heat discharge using aster image and meteorological data: Case study in Beijing metropolitan area, *J. Appl. Remote Sens.*, *6*(1), 63,551–63,559, doi:10.1117/1.JRS.6.063559.

Hu, L. Q., and N. A. Brunsell (2013), The impact of temporal aggregation of land surface temperature data for surface urban heat island (SUHI) monitoring, *Remote Sens. Environ.*, *134*, 162–174, doi:10.1016/j.rse.2013.02.022.

Huang, J. P., H. R. Cho, and G. R. North (1996), Applications of the cyclic spectral analysis to the surface temperature fluctuations in a stochastic climate model and a GCM simulation, *Atmos. Ocean*, *34*(4), 627–646, doi:10.1080/07055900.1996.9649580.

Hylleberg, S. (1994), *Modeling Seasonal Variation*, Oxford Univ. Press, Oxford, U. K.

Imhoff, M. L., P. Zhang, R. E. Wolfe, and L. Bounoua (2010), Remote sensing of the urban heat island effect across biomes in the continental USA, *Remote Sens. Environ.*, *114*(3), 504–513, doi:10.1016/j.rse.2009.10.008.

Jackson, T. J., D. Chen, M. Cosh, F. Li, M. Anderson, C. Walthall, P. Doriaswamy, and E. R. Hunt (2004), Vegetation water content mapping using Landsat data derived normalized difference water index for corn and soybeans, *Remote Sens. Environ.*, *92*(4), 475–482, doi:10.1016/j.rse.2003.10.021.

Jamali, S., P. Jönsson, L. Eklundh, J. Ardö, and J. Seaquist (2015), Detecting changes in vegetation trends using time series segmentation, *Remote Sens. Environ.*, *156*, 182–195, doi:10.1016/j.rse.2014.09.010.

Jenerette, D. G., S. L. Harlan, A. Brazel, N. Jones, L. Larsen, and W. L. Stefanov (2007), Regional relationships between surface temperature, vegetation, and human settlement in a rapidly urbanizing ecosystem, *Landscape Ecol.*, *22*(3), 353–365, doi:10.1007/s10980-006-9032-z.

Jiménez-Muñoz, J. C., and J. A. Sobrino (2003), A generalized single-channel method for retrieving land surface temperature from remote sensing data, *J. Geophys. Res.*, *108*(D22), 4688, doi:10.1029/2003JD003480.

Jin, M. L., W. Kessomkiat, and G. Pereira (2011), Satellite-observed urbanization characters in Shanghai, China: Aerosols, urban heat island effect, and land-atmosphere interactions, *Remote Sens.*, *3*(1), 83–99, doi:10.3390/rs3010083.

Jönsson, P., and L. Eklundh (2002), Seasonality extraction by function-fitting to time series of satellite sensor data, *IEEE Trans. Geosci. Remote Sens.*, *40*, 1824–1832, doi:10.1109/TGRS.2002.802519.

Julien, Y., and J. A. Sobrino (2012), Correcting AVHRR long term data record V3 estimated LST from orbital drift effects, *Remote Sens. Environ.*, *123*, 207–219, doi:10.1016/j.rse.2012.03.016.

Kim, Y., and J. Baik (2002), Maximum urban heat island intensity in Seoul, *J. Appl. Meteorol.*, *41*, 651–659, doi:10.1175/1520-0450(2002)041<0651:MUHIII>2.0.CO;2.

Knutti, R., G. A. Meehl, M. R. Allen, and D. A. Stainforth (2006), Constraining climate sensitivity from the seasonal cycle in surface temperature, *J. Clim.*, *19*(17), 4224–4233, doi:10.1175/JCLI3865.1.

Kusaka, H., and F. Kimura (2004), Thermal effects of urban canyon structure on the nocturnal heat island: Numerical experiment using a mesoscale model coupled with an urban canopy model, *J. Appl. Meteorol.*, *43*(12), 1899–1910, doi:10.1175/JAM2169.1.

Laskar, J., F. Joutel, and F. Boudin (1993), Orbital, precessional, and insolation quantities for the Earth from −20 MYR to +10 MYR, *Astron. Astrophys.*, *270*(1–2), 522–533.

Lee, D. (1991), Urban-rural humidity differences in London, *Int. J. Climatol.*, *11*(5), 577–582, doi:10.1002/joc.3370110509.

Li, Z. L., B. H. Tang, H. Wu, H. Z. Ren, G. J. Yan, Z. M. Wan, I. F. Trigo, and J. A. Sobrino (2013), Satellite-derived land surface temperature: Current status and perspectives, *Remote Sens. Environ.*, *131*, 14–37, doi:10.1016/j.rse.2012.12.008.

Liu, W., H. You, and J. Dou (2009), Urban-rural humidity and temperature differences in the Beijing area, *Theor. Appl. Climatol.*, *96*(3-4), 201–207, doi:10.1007/s00704-008-0024-6.

Liu, Y., T. Hiyama, and Y. Yamaguchi (2006), Scaling of land surface temperature using satellite data: A case examination on ASTER and MODIS products over a heterogeneous terrain area, *Remote Sens. Environ.*, *105*(2), 115–128, doi:10.1016/j.rse.2006.06.012.

Lo, C. P., D. A. Quattrochi, and J. C. Luvall (1997), Application of high-resolution thermal infrared remote sensing and GIS to assess the urban heat island effect, *Int. J. Remote Sens.*, *18*(2), 287–304, doi:10.1080/014311697219079.

Lu, D., P. Mausel, E. Brondízio, and E. Moran (2004), Change detection techniques, *Int. J. Remote Sens.*, *25*(12), 2365–2401, doi:10.1080/0143116031000139863.

Luvall, J. C., and H. R. Holbo (1989), Measurement of short-term thermal responses of coniferous forest canopies using thermal scanner data, *Remote Sens. Environ.*, *27*, 1–10, doi:10.1016/0034-4257(89)90032-1.

Luvall, J. C., D. A. Quattrochi, D. L. Rickman, and M. G. Estes Jr. (2015), Boundary layer (atmospheric) and air pollution | urban heat islands, in *Encyclopedia of Atmospheric Sciences*, vol. 1, pp. 310–318, Elsevier, Amsterdam, doi:10.1016/B978-0-12-382225-3.00442-4.

Mackey, C. W., X. H. Lee, and R. B. Smith (2012), Remotely sensing the cooling effects of city scale efforts to reduce urban heat island, *Build. Environ.*, *49*, 348–358, doi:10.1016/j.buildenv.2011.08.004.

Mcdonald, R. I., P. Green, D. Balk, B. M. Fekete, C. Revenga, M. Todd, and M. Montgomery (2011), Urban growth, climate change, and freshwater availability, *Proc. Natl. Acad. Sci. U.S.A.*, *108*(15), 6312–6317, doi:10.1073/pnas.1011615108/-/DCSupplemental.

Menenti, M., S. Azzali, W. Verhoef, and R. van Swol (1993), Mapping agroecological zones and time lag in vegetation growth by means of Fourier analysis of time series of NDVI images, *Adv. Space Res.*, *13*(5), 233–237, doi:10.1016/0273-1177(93)90550-U.

Mitraka, Z., N. Chrysoulakis, Y. Kamarianakis, P. Partsinevelos, and A. Tsouchlaraki (2012), Improving the estimation of urban surface emissivity based on sub-pixel classification of high resolution satellite imagery, *Remote Sens. Environ.*, *117*, 125–134, doi:10.1016/j.rse.2011.06.025.

Nichol, J. (2005), Remote sensing of urban heat islands by day and night, *Photogramm. Eng. Remote Sens.*, *71*(5), 613–621, doi:10.14358/PERS.71.5.613.

Oke, T. R. (1982), The energetic basis of the urban heat island, *Q. J. R. Meteorol. Soc.*, *108*(455), 1–24, doi:10.1002/qj.49710845502.

Oke, T. R. (1988), The urban energy balance, *Prog. Phys. Geogr.*, *12*, 471–508, doi:10.1177/030913338801200401.

Oke, T. R., G. T. Johnson, D. G. Steyn, and I. D. Watson (1991), Simulation of surface urban heat islands under 'ideal' conditions at night part 2: Diagnosis of causation, *Boundary Layer Meteorol.*, *56*(4), 339–358, doi:10.1007/BF00119211.

Ottle, C., and M. Stoll (1993), Effect of atmospheric absorption and surface emissivity on the determination of land surface temperature from infrared satellite data, *Int. J. Remote Sens.*, *14*(10), 2025–2037, doi:10.1080/01431169308954018.

Parey, S., T. T. H. Hoang, and D. Dacunha-Castelle (2013), The importance of mean and variance in predicting changes in temperature extremes, *J. Geophys. Res. Atmos.*, *118*, 8285–8296, doi:10.1002/jgrd.50629.

Peng, S., S. Piao, P. Ciais, P. Friedlingstein, C. Ottle, F. Bréon, H. Nan, L. Zhou, and R. B. Myneni (2012), Surface urban heat island across 419 global big cities, *Environ. Sci. Technol.*, *46*(2), 696–703, doi:10.1021/es2030438.

Pinheiro, A. C. T., J. L. Privette, R. Mahoney, and C. J. Tucker (2004), Directional effects in a daily AVHRR land surface temperature dataset over Africa, *IEEE Trans. Geosci. Remote Sens.*, *42*(9), 1941–1954, doi:10.1109/TGRS.2004.831886.

Pinheiro, A. C. T., J. L. Privette, and P. Guillevic (2006), Modeling the observed angular anisotropy of land surface temperature in a Savanna, *IEEE Trans. Geosci. Remote Sens.*, *44*(4), 1036–1047, doi:10.1109/TGRS.2005.863827.

Prata, A. J., V. Caselles, C. Coll, J. A. Sobrino, and C. Ottlé (1995), Thermal remote sensing of land surface temperature from satellites: Current status and future prospects, *Remote Sens. Rev.*, *12*(3–4), 175–224, doi:10.1080/02757259509532285.

Price, J. C. (1991), Timing of NOAA afternoon passes, *Int. J. Remote Sens.*, *12*(1), 193–198, doi:10.1080/01431169108929644.

Quan, J., Y. Chen, W. Zhan, J. Wang, J. Voogt, and M. Wang (2014a), Multi-temporal trajectory of the urban heat island centroid in Beijing, China based on a Gaussian volume model, *Remote Sens. Environ.*, *149*, 33–46, doi:10.1016/j.rse.2014.03.037.

Quan, J., Y. Chen, W. Zhan, J. Wang, J. Voogt, and J. Li (2014b), A hybrid method combining neighborhood information from satellite data with modeled diurnal temperature cycles over consecutive days, *Remote Sens. Environ.*, *155*, 257–274, doi:10.1016/j.rse.2014.08.034.

Quattrochi, D. A., and J. C. Luvall (1999), Thermal infrared remote sensing for analysis of landscape ecological processes: Methods and applications, *Landscape Ecol.*, *14*, 577–598, doi:10.1023/A:1008168910634.

Quattrochi, D. A., and J. C. Luvall (2009), Thermal remote sensing in earth science research, in *The SAGE Handbook of Remote Sensing*, edited by T. A. Warner, M. Duane Nelis, and G. M. Foody, pp. 64–78, SAGE Publ., Ltd, London.

Ren, H., G. Yan, L. Chen, and Z. Li (2011), Angular effect of MODIS emissivity products and its application to the split-window algorithm, *ISPRS J. Photogramm. Remote Sens.*, *66*, 498–507, doi:10.1016/j.isprsjprs.2011.02.008.

Rizwan, A. M., Y. C. L. Dennis, and C. Liu (2008), A review on the generation, determination and mitigation of urban heat island, *J. Environ. Sci. China*, *20*, 120–128, doi:10.1016/S1001-0742(08)60019-4.

Roerink, G. J., M. Menenti, and W. Verhoef (2000), Reconstructing cloudfree NDVI composites using Fourier analysis of time series, *Int. J. Remote Sens.*, *21*(9), 1911–1917, doi:10.1080/014311600209814.

Sailor, D. J., and L. Lu (2004), A top-down methodology for developing diurnal and seasonal anthropogenic heating profiles for urban areas, *Atmos. Environ.*, *38*(17), 2737–2748, doi:10.1016/j.atmosenv.2004.01.034.

Santer, B. D., T. M. L. Wigley, J. S. Boyle, D. J. Gaffen, J. J. Hnilo, D. Nychka, D. E. Parker, and K. E. Taylor (2000), Statistical significance of trends and trend differences in layer-average atmospheric temperature time series, *J. Geophys. Res.*, *105*, 7337–7356, doi:10.1029/1999JD901105.

Schwarz, N., S. Lautenbach, and R. Seppelt (2011), Exploring indicators for quantifying surface urban heat islands of European cities with MODIS land surface temperatures, *Remote Sens. Environ.*, *115*(12), 3175–3186, doi:10.1016/j.rse.2011.07.003.

Small, C. (2012), Spatiotemporal dimensionality and time-space characterization of multitemporal imagery, *Remote Sens. Environ.*, *124*, 793–809, doi:10.1016/j.rse.2012.05.031.

Snyder, W. C., Z. Wan, Y. Zhang, and Y. Feng (1998), Classification-based emissivity for land surface temperature measurement from space, *Int. J. Remote Sens.*, *19*(14), 2753–2774, doi:10.1080/014311698214497.

Sobrino, J. A., Y. Julien, M. Atitar, and F. Nerry (2008), NOAA-AVHRR orbital drift correction from solar zenithal angle data, *IEEE Trans. Geosci. Remote Sens.*, *46*(12), 4014–4019, doi:10.1109/TGRS.2008.2000798.

Stathopoulou, M., C. Cartalis, and I. Keramitsoglou (2004), Mapping micro-urban heat islands using NOAA/AVHRR images and CORINE land cover: An application to coastal cities of Greece, *Int. J. Remote Sens.*, *25*(12), 2301–2316, doi:10.1080/01431160310001618725.

Stathopoulou, M., C. Cartalis, and M. Petrakis (2007), Integrating Corine Land Cover data and Landsat TM for surface emissivity definition: Application to the urban area of Athens, Greece, *Int. J. Remote Sens.*, *28*(15), 3291–3304, doi:10.1080/01431160600993421.

Stine, A. R., P. Huybers, and I. Y. Fung (2009), Changes in the phase of the annual cycle of surface temperature, *Nature*, *457*(7228), 435–440, doi:10.1038/nature07675.

Thanasis, V., B. Efthimia, and K. Dimitris (2011), Estimation of linear trend onset in time series, *Simul. Modell. Pract. Theory*, *19*, 1384–1398, doi:10.1016/j.simpat.2011.02.006.

Thomson, D. J. (1995), The seasons, global temperature, and precession, *Science*, *268*, 59, doi:10.1126/science.268.5207.59.

Tiangco, M., A. M. F. Lagmay, and J. Argete (2008), ASTER-based study of the night-time urban heat island effect in Metro Manila, *Int. J. Remote Sens.*, *29*(10), 2799–2818, doi:10.1080/01431160701408360.

Tran, H., D. Uchihama, S. Ochi, and Y. Yasuoka (2006), Assessment with satellite data of the urban heat island effects in Asian mega cities, *Int. J. Appl. Earth Obs. Geoinform.*, *8*(1), 34–48, doi:10.1016/j.jag.2005.05.003.

Unkašević, M., O. Jovanović, and T. Popović (2001), Urban-suburban/rural vapour pressure and relative humidity differences at fixed hours over the area of Belgrade city, *Theor. Appl. Climatol.*, *68*(1–2), 67–73, doi:10.1007/s007040170054.

Verbesselt, J., R. Hyndman, G. Newnham, and D. Culvenor (2010), Detecting trend and seasonal changes in satellite image time series, *Remote Sens. Environ.*, *114*(1), 106–115, doi:10.1016/j.rse.2009.08.014.

Vergni, L., and F. Todisco (2011), Spatio-temporal variability of precipitation, temperature and agricultural drought indices in Central Italy, *Agric. For. Meteorol.*, *151*(3), 301–313, doi:10.1016/j.agrformet.2010.11.005.

Verhoef, W., M. Menenti, and S. Azzali (1996), A colour composite of NOAA-AVHRR-NDVI based on time series analysis (1981–1992), *Int. J. Remote Sens.*, *17*(2), 231–235, doi:10.1080/01431169608949001.

Voogt, J. A., and T. R. Oke (2003), Thermal remote sensing of urban climates, *Remote Sens. Environ.*, *86*(3), 370–384, doi:10.1016/S0034-4257(03)00079-8.

Wan, Z. (1999), *MODIS Land-Surface Temperature Algorithm Theoretical Basis Document*, NASA/GSFC, Greenbelt, Md.
Wan, Z. M. (2014), New refinements and validation of the collection-6 MODIS land-surface temperature/emissivity product, *Remote Sens. Environ.*, *140*, 36–45, doi:10.1016/j.rse.2013.08.027.
Wan, Z. M., and J. Dozier (1996), A generalized split-window algorithm for retrieving land-surface temperature from space, *IEEE Trans. Geosci. Remote Sens.*, *34*(4), 892–905, doi:10.1109/36.508406.
Wan, Z. M., and Z. L. Li (2008), Radiance-based validation of the V5 MODIS land-surface temperature product, *Int. J. Remote Sens.*, *29*(17–18), 5373–5395, doi:10.1080/01431160802036565.
Wang, J., K. Wang, and P. Wang (2007), Urban heat (or cool) island over Beijing from MODIS land surface temperature, *J. Remote Sens.*, *11*(3), 330–339, doi:10.11834/jrs.20070346.
Wang, K., Z. Li, and M. Cribb (2006), Estimation of evaporative fraction from a combination of day and night land surface temperatures and NDVI: A new method to determine the Priestley–Taylor parameter, *Remote Sens. Environ.*, *102*(3–4), 293–305, doi:10.1016/j.rse.2006.02.007.
Wang, K. C., P. C. Wang, J. M. Liu, M. Sparrow, S. Haginoya, and X. J. Zhou (2005), Variation of surface albedo and soil thermal parameters with soil moisture content at a semi-desert site on the western Tibetan plateau, *Boundary Layer Meteorol.*, *116*, 117–129, doi:10.1007/s10546-004-7403-z.
Wang, X., H. Xie, and T. Liang (2008), Evaluation of MODIS snow cover and cloud mask and its application in Northern Xinjiang, China, *Remote Sens. Environ.*, *112*, 1497–1513, doi:10.1016/j.rse.2007.05.016.
Watts, L. M., and S. W. Laffan (2014), Effectiveness of the BFAST algorithm for detecting vegetation response patterns in a semi-arid region, *Remote Sens. Environ.*, *154*, 234–245, doi:10.1016/j.rse.2014.08.023.
Weng, Q. H., and P. Fu (2014), Modeling annual parameters of clear-sky land surface temperature variations and evaluating the impact of cloud cover using time series of Landsat TIR data, *Remote Sens. Environ.*, *140*, 267–278, doi:10.1016/j.rse.2013.09.002.
Xiong, X., A. Angal, S. Madhavan, D. Link, X. Geng, B. Wenny, A. Wu, H. Chen, and V. Salomonson (2014), MODIS instrument operation and calibration improvements, in *IGARSS, Quebec, Canada*, pp. 1385–1388, IEEE, Piscataway, N. J., doi:10.1109/IGARSS.2014.6946693.
Yang, J. X., and Y. P. Wang (2011), Estimating evapotranspiration fraction by modeling two dimensional space of NDVI/albedo and day-night land surface temperature difference: A comparative study, *Adv. Water Resour.*, *34*(4), 512–518, doi:10.1016/j.advwatres.2011.01.006.
Yang, W., B. Chen, and X. Cui (2014), High-resolution mapping of anthropogenic heat in China from 1992 to 2010, *Int. J. Environ. Res. Publ. Health*, *11*(4), 4066, doi:10.3390/ijerph110404066.
Yuan, F., and M. E. Bauer (2007), Comparison of impervious surface area and normalized difference vegetation index as indicators of surface urban heat island effects in Landsat imagery, *Remote Sens. Environ.*, *106*(3), 375–386, doi:10.1016/j.rse.2006.09.003.
Zeileis, A., C. Kleiber, W. Krämer, and K. Hornik (2003), Testing and dating of structural changes in practice, *Comput. Stat. Data Anal.*, *44*, 109–123, doi:10.1016/S0167-9473(03)00030-6.
Zhan, W., J. Zhou, W. Ju, M. Li, I. Sandholt, J. Voogt, and C. Yu (2014a), Remotely sensed soil temperatures beneath snow-free skin-surface using thermal observations from tandem polar-orbiting satellites: An analytical three-time-scale model, *Remote Sens. Environ.*, *143*, 1–14, doi:10.1016/j.rse.2013.12.004.
Zhan, W., W. Ju, S. Hai, G. Ferguson, J. Quan, C. Tang, Z. Guo, and F. Kong (2014b), Satellite-derived subsurface urban heat island, *Environ. Sci. Technol.*, *48*, 12,134–12,140, doi:10.1021/es5021185.
Zhang, G. P., and M. Qi (2005), Neural network forecasting for seasonal and trend time series, *Eur. J. Oper. Res.*, *160*(2), 501–514, doi:10.1016/j.ejor.2003.08.037.
Zhao, L., X. H. Lee, R. B. Smith, and K. Oleson (2014), Strong contributions of local background climate to urban heat islands, *Nature*, *511*, 216–219, doi:10.1038/nature13462.
Zhou, D. C., S. Q. Zhao, S. G. Liu, L. X. Zhang, and C. Zhu (2014), Surface urban heat island in China's 32 major cities: Spatial patterns and drivers, *Remote Sens. Environ.*, *152*, 51–61, doi:10.1016/j.rse.2014.05.017.
Zhou, J., Y. Chen, J. Wang, and W. Zhan (2011), Maximum nighttime urban heat island (UHI) intensity simulation by integrating remotely sensed data and meteorological observations, *IEEE J. Sel. Top. Appl. Earth Obs. Remote Sens.*, *4*(1), 138–146, doi:10.1109/JSTARS.2010.2070871.
Zhou, J., Y. Chen, X. Zhang, and W. Zhan (2013), Modeling the diurnal variations of urban heat islands with multi-source satellite data, *Int. J. Remote Sens.*, *34*(21), 7568–7588, doi:10.1080/01431161.2013.821576.